Karlsruhe Institute of Technology

Institute of Photonics and Quantum Electronics (IPQ)
Head of Institute
Prof. Dr. Christian Koos

Master Thesis No. M-

Ahmed Shariful Alam

Design, Fabrication and Characterization of Capacitively Coupled Silicon-Organic Hybrid Modulators

Start:	15.05.2017
End:	15.11.2017
Referent:	Prof. Dr. Christian Koos Institute of Photonics and Quantum Electronics Institute of Microstructure Technology
Supervisor:	M.Sc. Sandeep Ummethala Institute of Photonics and Quantum Electronics Institute of Microstructure Technology

Abstract

Silicon-organic hybrid (SOH) modulators [1] offer fast and efficient electro-optic modulation with very small footprints. Traditional SOH modulators suffer from bandwidth limitation due to the higher RC time constant that originates from the resistive coupling of the RF signal. In the current thesis, we propose a new modulator concept establishing a capacitive coupling of the RF signal as opposed to the resistive one in the conventional SOH modulators and hence the name capacitively coupled SOH (CC-SOH) modulator. A high-κ dielectric, $BaTiO_3$ is characterized in optical and in RF regime and later used to design capacitively coupled SOH modulator. The fabicated CCSOH is characterized to have a flat frequency response up to 65 GHz indicating that the 3-dB bandwidth is at least 3 times higher than the SOH modulators.

Declaration

I hereby declare that I wrote my master thesis on my own and that I have followed the regulations relating to good scientific practice of the Karlsruhe Institute of Technology (KIT) in its latest form. I did not use any unacknowledged sources or means and I marked all references I used literally or by content.

Karlsruhe, 15th November, 2017

Ahmed Shariful Alam

Contents

List of Figures

Chapter 1

Introduction

Data traffic is growing exponentially in communication networks across the world. Fiber optic communication networks currently handle more than 50% of the traffic form the backbone for global communication. To keep up with the current demands, it is imperative to increase the capacity of the optical communication links [2]. One of the key elements that decides the data rate of a fiber-optic link is an electro-optic (EO) modulator that encodes the digital bit stream onto an optical signal [3, 4].

Modern electro-optic modulators exploit second-order nonlinearities of different electro-optic materials. Nonlinear crystalline materials like di-deuterium phosphate (KD^*P) [5,6], potassium titanyl phosphate (KTP) [7], lithium niobate ($LiNbO_3$) [8] etc. are used to fabricate different electro-optic modulators. Due to poor electro-optic properties of these materials, these modulators have large footprints and are bulky [9, 10]. Such modulators are not still commercially available in smaller size sand are difficult to co-integrate them with electronics which is completely built on silicon. Hence silicon photonics has gained great interest in the recent years which allows a seamless integration of optics and electronics on the same platform.

Different EO effects such as the Kerr effect & the Franz-Keldysh effect are poor in silicon and the Pockels effect is absent in bulk silicon [11]. Silicon modulators based on the plasma dispersion effect, by which both the real and the imaginary parts of the refractive index could be manipulated by changing the free career concentration are used for optical modulation [12]. These modulators are known as the carrier accumulation modulators (well known as the p-n modulators). The p-n modulator is CMOS compatible and a good candidate to make photonic-electronic co-integration possible. However, the signal is distorted during the modulation due the amplitude-phase coupling. Moreover, these modulators consume relatively high amount of energy (∼5000 fJ/bit) [13]. So a new architecture of silicon modulator was needed to be introduced.

Stronger EO properties have been observed in engineered organic polymers [14, 15] which opened new possibilities for the electro-optic modulation in silicon photonics. Silicon-organic hybrid (SOH) [16] and plasmonic-organic hybrid (POH) [17] modulators have been already demonstrated using different EO polymers. Though the POH modulators have higher modulation bandwidth, the SOH modulators show better performance in terms of power efficiency and insertion loss [18]. But the SOH modulators suffer from bandwidth limitation for the RC time constant which results from the resistive coupling of the RF signal [19, 20]. Though the bandwidth can be enhanced significantly by applying a very high gate voltage [21], this might not be a feasible solution in practice. So this master thesis aims on a new architecture of SOH modulator, named as the capacitively coupled SOH (CC-SOH) modulator, which is expected to improve its bandwidth significantly.

This thesis is organized in several chapters. In Chapter 2, the concept of SOH modulators that forms the basis for the new architecture of CC-SOH is presented. Additionally, this chapter contains a literature review on the thin films with high dielectric constant (high-κ) material ($BaTiO_3$) and the dielectric constant extraction process. Chapter 3 explains the sputtering of $BaTiO_3$ thin films and shows experimental results of the optical & RF characterization of the sputtered $BaTiO_3$ thin films. Afterwards, the optical & RF simulations for designing the CC-SOH modulators and the device fabrication procedure is presented in Chapter 4. Later on, the transmission measurements and the bandwidth measurements of the fabricated modulators is presented in Chapter 5.

Chapter 2

Theoretical Background

The chapter starts with Section 2.1 which briefly discuss the second order nonlinearities required for EO modulation. An overview of the SOH modulator and its bandwidth limitations is explained in Section 2.2. Afterwards, the operating principle of CC-SOH modulator is explained in Section 2.3. A short literature review on the $BaTiO_3$ thin films, which is used as a high-κ dielectric, is presented in Section 2.4. Finally, the theory of dielectric constant extraction procedure of these thin films is discussed in Section 2.5.

2.1 Nonlinear Optics and EO Effects

The SOH modulators modulate the light exploiting the Pockels effect in highly nonlinear EO chromophores. The field of nonlinear optics has to be explained in order to understand the background of the thesis. The linear & nonlinear polarization, the Pockels effect and the principles of EO modulation have been discussed briefly in this section. For a detailed description of nonlinear optics and the EO effects in optical media, the reader is suggested to go through the textbook of R. W. Boyd [22].

2.1.1 Linear and Nonlinear Polarization

When an electromagnetic wave with a time and space dependent electric field $\mathbf{E}(\mathbf{r},t)$ propagates through an optical medium, the bound charges in the medium (nuclei and the electrons) gets separated slightly. This induces a local electric dipole moment. Then the electric field displacement, $\mathbf{D}(\mathbf{r},\mathrm{t})$ can be defined as,

$$\mathbf{D}(\mathbf{r},t) = \epsilon_0 \mathbf{E}(\mathbf{r},t) + \mathbf{P}(\mathbf{r},t) \tag{2.1}$$

The vacuum permittivity is $\epsilon_0 = 8.854 \times 10^{-12}$ As/Vm. $\mathbf{P}(\mathbf{r},\mathrm{t})$ is the time dependent electric polarization which is actually the response of the optical medium as a result of the electromagnetic wave propagation through it. The relation between $\mathbf{E}(\mathrm{r,t})$ and $\mathbf{P}(\mathbf{r},\mathrm{t})$ can be expresses by a Volterra series.

$$\begin{aligned}
\mathbf{P}(\mathbf{r},t) = {}& \epsilon_0 \int_0^\infty \underline{\chi}^{(1)}(\mathbf{r},t-t')\mathbf{E}(\mathbf{r},t')dt' \\
&+ \epsilon_0 \int_0^\infty \int_0^\infty \underline{\chi}^{(2)}(\mathbf{r},t-t',t-t'') : \mathbf{E}(\mathbf{r},t')\mathbf{E}(\mathbf{r},t'')dt'dt'' \\
&+ \epsilon_0 \int_0^\infty \int_0^\infty \int_0^\infty \underline{\chi}^{(3)}(\mathbf{r},t-t',t-t'',t-t''')\vdots\mathbf{E}(\mathbf{r},t')\mathbf{E}(\mathbf{r},t'')\mathbf{E}(\mathbf{r},t''')dt'dt''dt''' \\
&+ \cdots
\end{aligned} \tag{2.2}$$

The possible temporal memory effects of the nonlinear optical medium is described by the causal influence function, $\underline{\chi}^{(n)}(t',t'',\cdots,t^{(n)})$ which is known as the electric susceptibility tensor of rank n+1. Due to causality, $\underline{\chi}^{(n)}(t',t'',\cdots,t^{(n)}) = 0$ for $t',t',,t^{(n)} < 0$ which is also confirmed by the lower boundaries of Equation 2.2. The electric susceptibility with rank 2, $\underline{\chi}^{(1)}$ is normally several orders of magnitude than the higher order electric susceptibilities. Hence the polarization term can be split into two parts, $\mathbf{P}(\mathbf{r},\mathrm{t})$ can be defined as,

$$\mathbf{P}(\mathbf{r},t) = \mathbf{P}^{\mathbf{L}}(\mathbf{r},t) + \mathbf{P}^{\mathbf{NL}}(\mathbf{r},t) \tag{2.3}$$

The linear polarization and the nonlinear polarizations take the form of Equation 2.4 and 2.5 respectively.

$$\mathbf{P}^{\mathbf{L}}(\mathbf{r},t) = \mathbf{P}^{(1)}(\mathbf{r},t) = \epsilon_0 \int_0^\infty \underline{\chi}^{(1)}(\mathbf{r},t-t')\mathbf{E}(\mathbf{r},t')dt' \tag{2.4}$$

$$
\begin{aligned}
\mathbf{P}^{\mathbf{NL}}(\mathbf{r},t) &= \sum_{n=2}^{\infty}\mathbf{P}^{(n)}(\mathbf{r},t) \\
&= \epsilon_0 \int_0^{\infty}\int_0^{\infty} \underline{\chi}^{(2)}(\mathbf{r},t-t',t-t'') : \mathbf{E}(\mathbf{r},t')\mathbf{E}(\mathbf{r},t'')dt'dt'' \\
&+ \epsilon_0 \int_0^{\infty}\int_0^{\infty}\int_0^{\infty} \underline{\chi}^{(3)}(\mathbf{r},t-t',t-t'',t-t''') \vdots \mathbf{E}(\mathbf{r},t')\mathbf{E}(\mathbf{r},t'')\mathbf{E}(\mathbf{r},t''')dt'dt''dt''' \\
&+ \cdots
\end{aligned}
\tag{2.5}
$$

Since the background of the thesis stands on the second order nonlinearity, $\mathbf{P}^{(2)}(\mathbf{r},t)$, from now the discussion will be restricted to the second order nonlinear effects ($\underline{\chi}^{(n)} = 0$ for $n > 2$). Considering that the input electric field has a frequency spectrum composed of discrete angular frequencies ω_1, ω_2, ..., ω_n the Fourier transform of Equation 2.5 (only for second order nonlinearity) becomes [22],

$$
\widetilde{P}_i^{(2)}(\omega_n+\omega_m) = \epsilon_0 \sum_{jk}\sum_{(nm)} \widetilde{\chi}^{(2)}_{ijk}(\omega_n+\omega_m;\omega_n,\omega_m)\widetilde{E}_j(\omega_n)\widetilde{E}_k(\omega_m) \tag{2.6}
$$

For the sake of readability, the spatial dependence has been eliminated in the quantities of Equation 2.6. $\widetilde{\chi}^{(2)}$ is the second order nonlinear electric susceptibility. The notation (nm) means that, the summation over the indices n and m includes only those sets of frequencies ω_n, ω_m which result in a frequency $\omega_n+\omega_m$. The indices i,j,k = 1,2,3 indicate the three orthogonal coordinates of the nonlinear optical medium.

2.1.2 Pockels Effect

The Pockels effect is a special type of second-order nonlinear effect. This is the linear EO effect which denotes the change of refractive index of the optical medium by means of applying a slowly varying electric field. The applied electric field is supposed to be slowly varying when it has a sufficiently low frequency, ω_m (couple of tens or hundreds of GHz) than the high frequency (ω_c) optical carrier field (the optical communication frequency of $\sim$ 193 THz). Then the change of refractive index occurs due to the interaction of the low frequency applied electric filed and the high frequency optical field in a material having a $\widetilde{\chi}^{(2)}$ tensor. Then Equation 2.6 can be re-written as,

$$
\widetilde{P}_i^{(2)}(\omega_c+\omega_m \approx \omega_c) = 2\epsilon_0 \sum_{jk} \widetilde{\chi}^{(2)}_{ijk}(\omega_c+\omega_m;\omega_c,\omega_m)\widetilde{E}_j(\omega_c)\widetilde{E}_k(\omega_m) \tag{2.7}
$$

The factor of 2 in Equation 2.7 comes as a result of the permutation symmetry of the input electric fields. This causes a permutation symmetry of the susceptibility tensor.

$$\widetilde{\chi}^{(2)}_{ijk}(\omega_c+\omega_m;\omega_c,\omega_m) = \widetilde{\chi}^{(2)}_{ijk}(\omega_c+\omega_m;\omega_m,\omega_c) \tag{2.8}$$

Applying the Einstein notation for sums and using the Equation 2.7 the electric field displacement, $\widetilde{D}_i(\omega_c)$ spectrum can be written as,

$$\widetilde{D}_i(\omega_c) = \epsilon_0\big(\delta_{ij} + \widetilde{\chi}^{(1)}_{ij}(\omega_c)\big) + 2\epsilon_0\widetilde{\chi}^{(2)}_{ijk}(\omega_c+\omega_m;\omega_c,\omega_m)\widetilde{E}_j(\omega_c)\widetilde{E}_k(\omega_m) \tag{2.9}$$

δ_{ij} is known as the Kronecker delta.

$$\delta_{ij} = \begin{cases} 1, & \text{if } i=j \\ 0, & \text{otherwise} \end{cases} \tag{2.10}$$

The low frequency applied electric field dependent electric permittivity of the second order nonlinear optical medium can be defined as,

$$\epsilon_{ij} = \epsilon_0\big(\delta_{ij} + \widetilde{\chi}^{(1)}_{ij} + 2\widetilde{\chi}^{(2)}_{ijk}\widetilde{E}_k(\omega_m)\big) = \epsilon_0(\epsilon_{r,ij} + \Delta\epsilon_{r,ij}) \tag{2.11}$$

The change of permittivity of the nonlinear optical medium upon applying a low frequency electric field,$\Delta\epsilon_{r,ij}$ is,

$$\Delta\epsilon_r = 2\widetilde{\chi}^{(2)}_{ijk}\widetilde{E}_k(\omega_m) \tag{2.12}$$

A special case is considered for the Equation 2.12 where both the applied low frequency electric field and the electric field of the optical field are polarized along the axis-3. $\widetilde{\chi}^{(2)}_{333}$ is assumed to be the dominant component of the electric permittivity tensor. In such case the change of permittivity is given by,

$$\Delta\epsilon_r = 2\widetilde{\chi}^{(2)}_{333}\widetilde{E}_3(\omega_m) \tag{2.13}$$

If the refractive index of the medium before applying the low frequency electric field is n and the change of the optical medium is Δn then,

$$\epsilon_r + \Delta\epsilon_r = (n+\Delta n)^2 \approx n^2 + 2n\Delta n \tag{2.14}$$

Comparing Equation 2.13 and 2.14 the expression for Pockels effect is found.

$$\Delta n = \frac{\Delta\epsilon_r}{2n} = \frac{\widetilde{\chi}^{(2)}_{333}}{n}\widetilde{E}_3(\omega_m) \tag{2.15}$$

According to the Equation 2.15, the change of refractive index of the optical medium is linearly proportional to the low frequency applied electric field. That is why the Pockels effect is also known as the linear EO effect. The EO coefficient, r_{ijk} is preferred over the second order susceptibility tensor, $\widetilde{\chi}^{(2)}_{ijk}$ while dealing with the EO modulation of the optical field. The change of the refractive index in terms of EO coefficient matrix is defined by [23],

$$\Delta n_{ij} = -\frac{1}{2} n_o^3 r_{ijk} \widetilde{E}_k(\omega_m \approx 0) \tag{2.16}$$

By comparing the Equation 2.15 and 2.16 a relation between the EO coefficient and the electric permittivity can be established.

$$r_{ijk} = -2\frac{\widetilde{\chi}^{(2)}_{ijk}}{n_o^4} \tag{2.17}$$

Considering the permutation symmetry of the input fields, the number of independent component of $\widetilde{\chi}^{(2)}_{ijk}$ and r_{ijk} is reduced to 18 from 27. The tensors $\widetilde{\chi}^{(2)}_{ijk}$ and r_{ijk} are expressed by contracted notations $\widetilde{\chi}^{(2)}_{ih}$ and r_{ih} respectively where,

$$h = \begin{cases} 1, & \text{for } jk = 11 \\ 2, & \text{for } jk = 22 \\ 3, & \text{for } jk = 33 \\ 4, & \text{for } jk = 23 \text{ or } 32 \\ 5, & \text{for } jk = 13 \text{ or } 31 \\ 6, & \text{for } jk = 12 \text{ or } 21 \end{cases} \tag{2.18}$$

2.1.3 Silicon Slot Waveguide

The conventional waveguides confine the optical field in optical media with higher refractive indices. Silicon slot waveguide is a special waveguide where the optical field is confined rather in a low-refractive index medium [24]. A silicon slot waveguide consists of two silicon rails (Figure 2.1). The gap between the two silicon rails is called the slot which can be as small as 100 nm. The material in the slot is known as the cladding material which has a lower refractive index than silicon ($n_c < n_{Si}$). If the normal components of the electric fields in the silicon rails and the cladding are $E^{(N)}_{Si}$ and $E^{(N)}_c$ then according to the boundary condition,

$$n_{Si}^2 E^{(N)}_{Si} = n_c^2 E^{(N)}_c \tag{2.19}$$

From the Equation 2.19 it is clearly visible that, there is an electric field discontinuity at the silicon-cladding interface. $E^{(N)}_c >> E^{(N)}_{Si}$ since $n_c < n_{Si}$. So a very high electric field

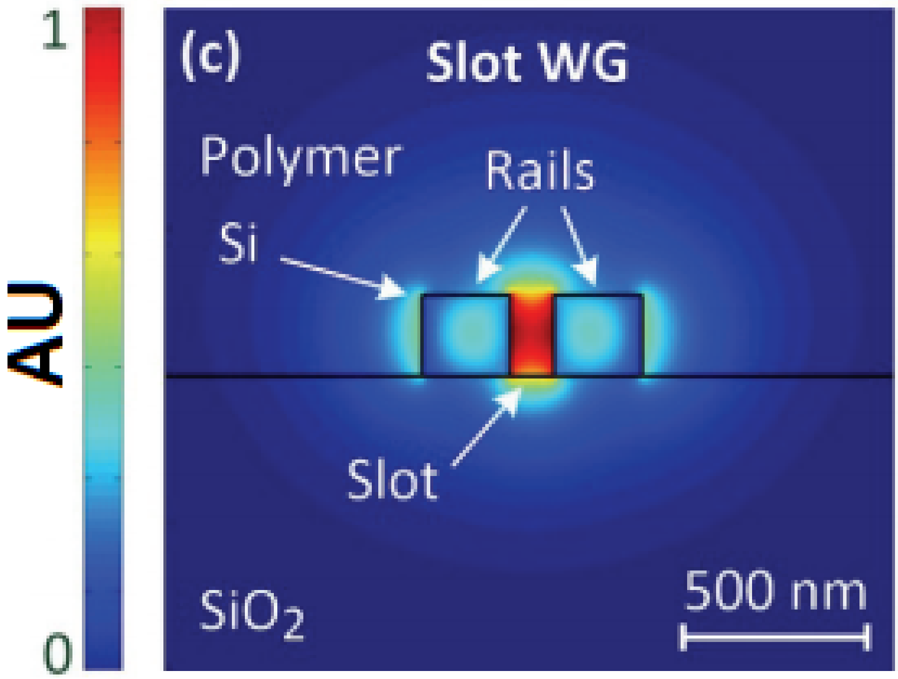

Figure 2.1: Cross-section of silicon slot waveguide [20]

confinement is achieved in the slot region which is also visible in the Figure 2.1. In an SOH modulator the cladding material is an organic EO polymer exhibiting second order nonlinearity.

2.1.4 EO Modulation

EO modulators exploit the second order nonlinearity of the optical medium upon application of a low frequency (ω_m) electric field, E_m. Depending upon the direction of E_m with respect to the direction of propagation of the optical signal, there exist two types of EO modulators longitudinal modulator and transverse modulator. For a longitudinal modulator E_m is applied parallel to the propagation direction of the optical field having a frequency of ω_c, whereas for the transverse modulator the direction of E_m is perpendicular to the propagation direction of the optical field. This section will be restricted to the discussion of the transverse modulator.

For a transverse modulator shown in Figure 2.2(a) the propagation direction of the optical field is considered along the z-axis (axis-3). So the field induced refractive index change

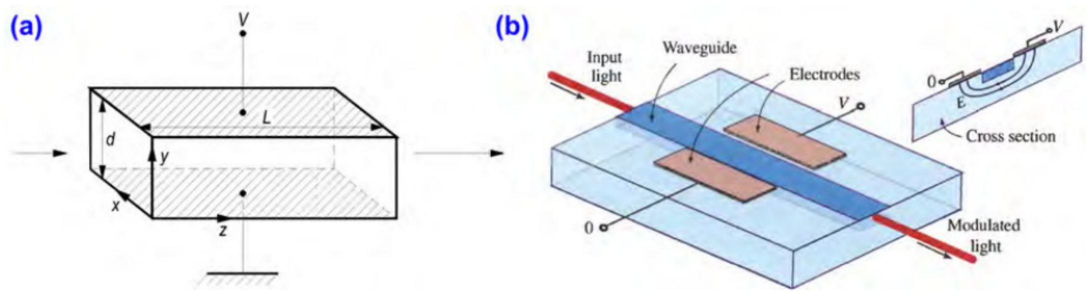

Figure 2.2: Transverse EO modulator. (a) Modulation of light propagating in the z-direction by applying electric field perpendicular to it. (b) A phase modulator [25]

can be given by,

$$\Delta n = -\frac{1}{2} n_o^3 r_{33} E_m \tag{2.20}$$

The corresponding phase shift, $\Delta\Phi$ accumulated along the propagation distance, L can be expressed by,

$$\Delta\Phi = -k_0 \Delta n L = \frac{1}{2} n_o^3 r_{33} E_m k_0 L = \frac{1}{2}\frac{\omega_c}{c} n_o^3 r_{33} E_m L = \frac{\pi}{\lambda_c} n_o^3 r_{33} E_m L \tag{2.21}$$

The modulating electric field E_m depends upon the externally applied voltage, V and the separation between the electrodes, d (Figure 2.2(a)).

$$E_m = \frac{V}{d} \tag{2.22}$$

This leads to a half-wave voltage, V_π,

$$V_\pi = \frac{d}{L}\frac{\lambda_c}{n_o^3 r_{33}} \tag{2.23}$$

Since this modulator is changing the phase of the optical field, it is called a phase modulator (Figure 2.2(b)).

2.2 Silicon-Organic Hybrid (SOH) Electro-optic Modulator

The silicon-organic hybrid (SOH) platform is a powerful technology where silicon photonics is combined with organic polymers to perform electro-optic modulation. The SOH platform

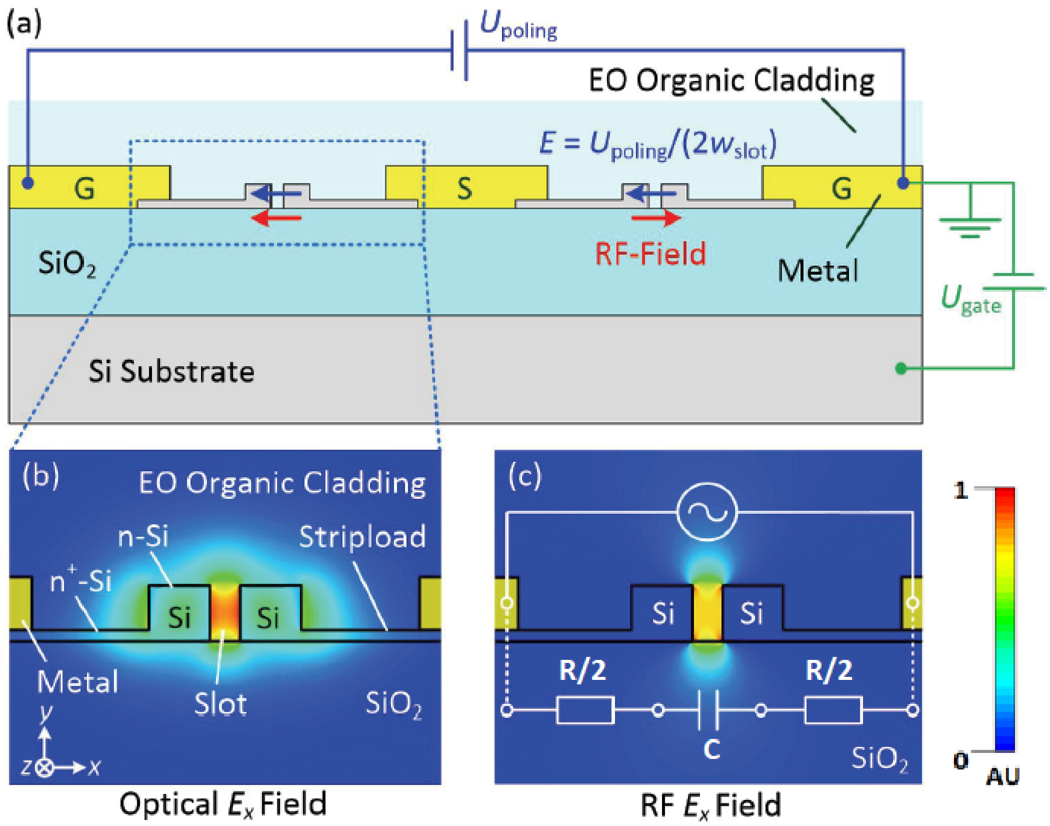

Figure 2.3: (a) Cross-section of a SOH Mach-Zehnder modulator, (b) optical field, (c) RF electric field [20]

has been successfully used to fabricate phase modulator [26], Mach-Zehnder modulator [27] and optical IQ modulator [28]. In this section, the working principle of SOH electro-optic modulator and its bandwidth limitations will be discussed.

2.2.1 Working Principle

The SOH modulator relies on CMOS technology for fabricating silicon slot waveguides and exploits nonlinear organic material in the slot region. The cross-sectional view of an SOH Mach-Zehnder electro-optic modulator is shown in Figure 2.3(a). Figure 2.3(b) clearly shows that the optical field confined within the slot region where the organic electro-optic material is deposited by spin coating. The RF electric filed is fed through a coplanar waveguide. The RF field is coupled to the slot region by the silicon striploads (n^+ Si). Normally the dipoles of the organic material are randomly oriented. So a poling field has to be applied to orient the dipoles to a desired direction with respect to the applied modulating field in order to maximize the electro-optic response.

The phase shift of the optical field confined within the slot in one arm of the SOH MZM after applying an RF electric field, E_m having an angular frequency, ω_m can be expressed by Equation 2.24.

$$\Delta\Phi = \frac{1}{2} n_{EO}^3 r_{33} \Gamma_{slot} E_m k_0 L = \frac{1}{2} \frac{\omega_c}{c} n_{EO}^3 r_{33} \Gamma_{slot} E_m L = \frac{\pi}{\lambda_c} n_{EO}^3 r_{33} \Gamma_{slot} E_m L \tag{2.24}$$

n_{EO} is the refractive index of the organic EO polymer and Γ_{slot} is the field interaction factor.

$$\Gamma_{slot} = \frac{c\epsilon_0 n_{EO} \iint\limits_{D_{slot}} \mid \underline{E}_{0,x} \mid^2 dxdy}{\iint\limits_{-\infty}^{+\infty} Re\big[\underline{E}_0(x,y) \times \underline{H}_0^*(x,y)\big].\vec{e}_z dxdy} \tag{2.25}$$

Here, $E_{0,x}$ is the x-component of the optical field. In Equation 2.25, the area integral of the numerator extends only over the slot region D_{slot} and the denominator is the area integral of the real part of the poynting vector over the whole surface normal to the propagation direction of the optical signal. If the slot width is w_{slot} and the external applied voltage is V then,

$$\Delta\Phi = \frac{\pi}{\lambda_c} \frac{V}{w_{slot}} n_{EO}^3 r_{33} \Gamma_{slot} L \tag{2.26}$$

Then half-wave voltage, resulting in a phase shift of π, V_π is,

$$V_\pi = \frac{\lambda_c w_{slot}}{n_{EO}^3 r_{33} \Gamma_{slot} L} \tag{2.27}$$

This is the expression for the V_π for a phase modulator. The orientation of the dipoles the direction of the applied RF filed are same in the left arm and are opposite in the right arm of the SOH MZM. As a consequence, the phase shifts of the optical fields in the two arms of the SOH MZM will hold opposite signs. Thus by a push-pull mechanism the electro-optic modulation is performed. For an MZM the V_π becomes half of the phase modulator.

$$V_\pi = \frac{\lambda_c w_{slot}}{2 n_{EO}^3 r_{33} \Gamma_{slot} L} \tag{2.28}$$

2.2.2 Bandwidth Limitation of SOH Modulator

The performance of an SOH modulator highly depends on the overlap of the optical field and the modulation electric field (RF field) in the organic electro-optic material. As described in Section 2.2.1, in the SOH modulator the optical field is confined in a narrow slot filled with organic electro-optic material and the confinement of the optical field depends upon the refractive index contrast of the silicon waveguide. The confinement of the RF field depends on the resistive coupling of the silicon rails through the doped silicon slabs. The finite conductance of the doped silicon slabs combined with the slot capacitance (Figure 2.3(c)) limit the bandwidth of the SOH modulator ($f_{3dB} \propto 1/\mathrm{RC}$). The resistances (R/2) and the capacitance (C) in the equivalent circuit come from the silicon striploads and electro-optic organic material respectively. For these reasons, this modulator might also be called as Resistively Coupled SOH Modulator.

2.3 Capacitively Coupled SOH (CC-SOH) Electro-optic Modulator

To overcome the bandwidth limitations of the conventional SOH modulator as explained in Section 2.2, a new coupling concept has been presented in the current work which replaces the resistive coupling of the RF field through a capacitively coupled RF field. This can be done by replacing the silicon slabs of the conventional SOH (resistively coupled) modulator by high-κ dielectric material. The new modulator is named as *capacitively coupled SOH (CC-SOH) modulator*. The cross-section of a CC-SOH Mach-Zehnder modulator is shown in Figure 2.4(a).

Silimilar to an SOH modulator, a CC-SOH modulator has a silicon slot waveguide fabricated on SOI platform. The buried oxide (SiO_2) layer and the organic electro-optic material define the lower cladding and the upper cladding respectively. Each silicon slot waveguide that form a Mach-Zehnder modulator is positioned between metal electrodes arranged in a ground-signal-ground (GSG) configuration. The high-κ material thin films are deposited in the gap between the electrodes and the rails that form the silicon slot waveguides. The high-κ material has to be chosen in such a way that, it has a very high dielectric constant at microwave frequency range (0.3-300 GHz) but has refractive indices lower than silicon core (silicon rails) at wavelengths around 1550 nm. The refractive index contrast at the interface of silicon and EO polymer causes electric field discontinuity of the hybrid TE mode leading to a E-field enhancement that is confined within slot (Figure 2.4(b)). If we consider the whole arrangement as lumped components then the high-κ material thin film will lead to a capacitance $C_{high-\kappa}$ and the EO polymer in the slot will lead to another capacitance C_{slot} (Figure 2.4(c)). If the material has sufficiently high dielectric

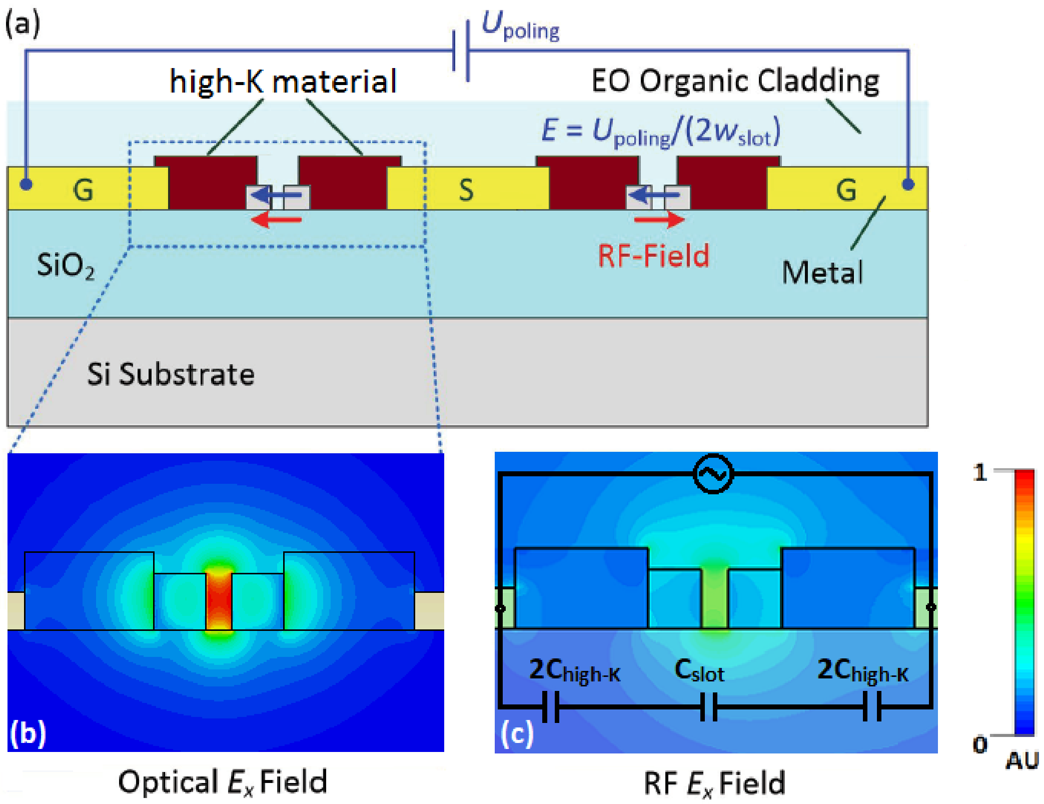

Figure 2.4: (a) Cross-section of a CC-SOH Mach-Zehnder modulator, (b) optical field, (c) RF electric field

constant at RF frequencies then $C_{high-\kappa}$ can be neglected which will maximize the RF electric field intensity in the slot. Thus the bandwidth of the modulator can be improved significantly.

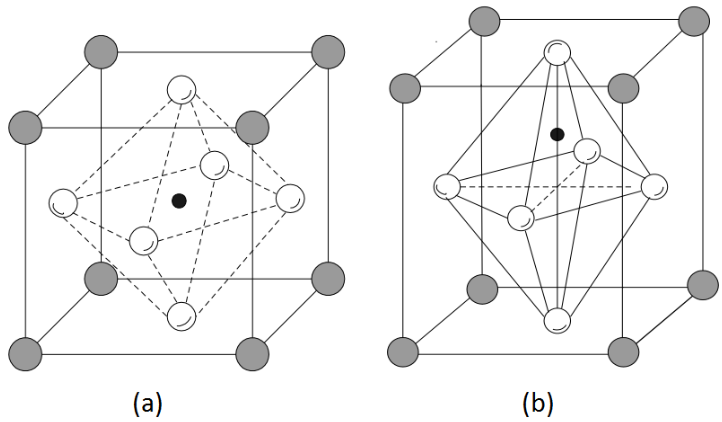

Figure 2.5: $BaTiO_3$ crystals, (a) Cubic lattice & (b) Tetragonal lattice

2.4 Choice of High-κ Dielectric Material

As discussed in section 2.3, a thin film of a material will be needed which has a very high dielectric constant in the microwave frequencies. The material should also have a lower refractive index at 1550 nm wavelength than silicon to fulfil the guiding mode condition of slot waveguide. For the current work Barium Titanate, $BaTiO_3$ (BTO) has been used as a high-κ dielectric material. In this section, the characteristics of $BaTiO_3$ will be discussed briefly.

2.4.1 Barium Titanate ($BaTiO_3$)

Thin films of Barium Titanate ($BaTiO_3$ or BTO) have received enormous attention in recent years for its uses in capacitors and its ferroelectric [29], piezoelectric [30] and EO [31] properties. BTO is a fundamental perovskite oxide with high dielectric constant and low loss in the microwave frequency regime. So various applications of BTO thin films have been possible in microelectronics and integrated optics technologies.

The high dielectric constant of BTO basically comes from its crystal structure. Generally the perovskite structure of $BaTiO_3$ exists in two crystallographic forms [32] - cubic lattice (Figure 2.5(a)) and tetragonal lattice (Figure 2.5(a)). Such crystalline thin films can be deposited by only epitaxial growth [33] or partial epitaxial growth followed by other deposition method such as, sputtering [34]. These films when grown epitaxially also have interesting electro-optic properties. BTO thin films can also be deposited by other methods such as hydrothermal synthesis [35], pulsed lased deposition [36,37] and sputtering [38,39]. Such films are normally distorted crystalline, polycrystalline or amorphous depending on the deposition conditions. So the dielectric constant and the loss of the thin film vary depending upon the deposition method and different deposition parameters as well as the film thickness. The deposition method and the dielectric properties of BTO thin film which is used in our experiments will be discussed in chapter 3.

2.5 Extraction of Dielectric Constant of Thin Films

Thin films often show different dielectric properties from the bulk materials. Again as mentioned in section 2.4, the dielectric constant and the loss of the thin film depends on the deposition method and deposition parameters. Besides thin films show different dielectric properties for different thicknesses.

There are a number of methods which can be used to determine the dielectric properties of a thin film. The most common methods are-

- Parallel plate method,
- Transmission line method,
- Transmission free space method and
- Resonant cavity method

The *parallel plate method* uses a parallel plate capacitor where the thin film is sandwiched between two electrodes (Figure 2.6). This method requires an impedance analyzer. The dielectric constant is measured from the capacitance measured by the impedance analyzer. But precision measurements are difficult for high frequencies and low loss materials using this method because of the measurement errors like the fringing capacitance [40]. So this method is suitable for low frequencies (lower than 1 GHz).

The *transmission line method* (Figure 2.7(b)) uses different types of transmission lines (Figure 2.7(a)) such as slotlines, coplanar waveguides, and microstrips etc. which are fabricated on top of the thin films. A vector network analyzer (VNA) measures the transmission and reflection of the transmission line which is eventually used to determine the

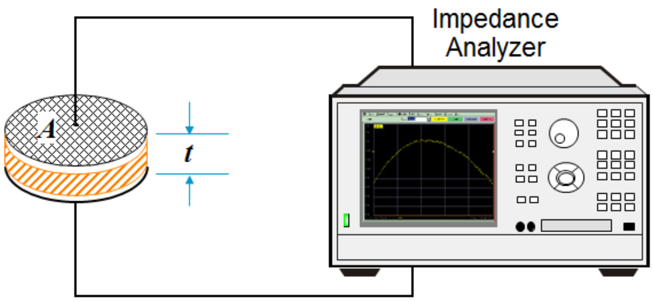

Figure 2.6: Parallel plate method

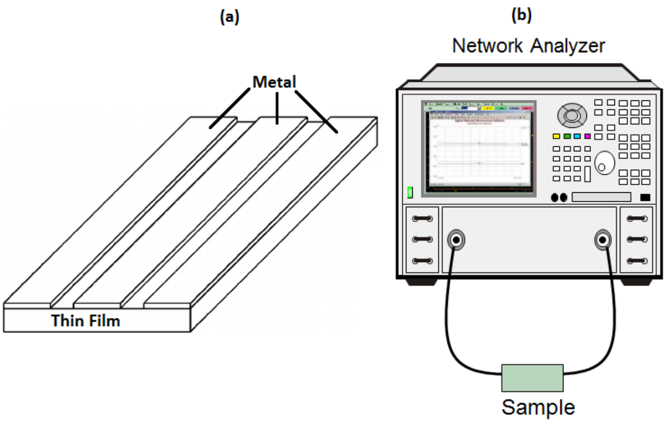

Figure 2.7: Transmission line method, (a) transmission line (coplanar waveguide), (b) the setup

dielectric properties of the thin film using different algorithms. The accuracy of measured dielectric property is not very precise but this method is quite useful for a very broad frequency range.

The *transmission free space method* [41] is similar to the transmission line method. This method uses two antennas and the thin film is placed between them as shown in Figure 2.8. The transmission and reflection are measured using a VNA and thus dielectric constant is measured. Similar kind of algorithms which are applied in *transmission line method* can be applied to this method as well to calculate the dielectric constant from the transmission and reflection spectra.

A resonant cavity (Figure 2.9(a)) is used to determine the dielectric constant of a thin film in the *resonant cavity method* [42]. If a microwave signal is applied to the cavity a

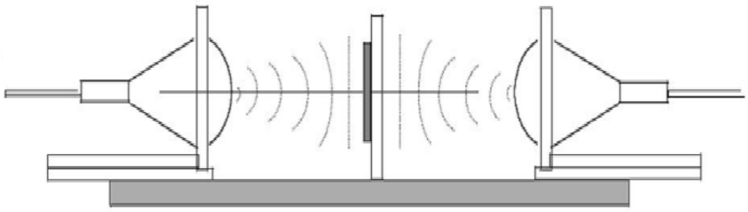

Figure 2.8: Transmission free space method

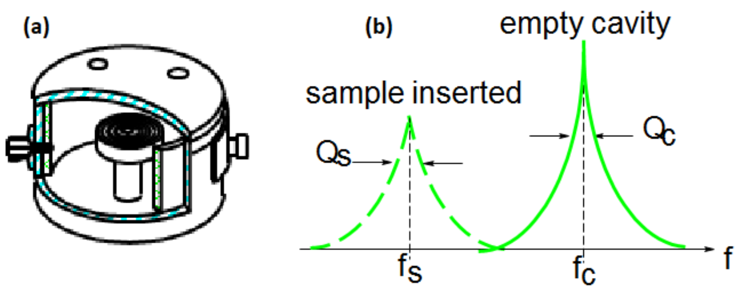

Figure 2.9: Resonant Cavity Method (a) The cavity and (b) the resonant frequencies of an empty cavity and a sample loaded cavity

resonance occurs. The resonant frequencies are different for an empty cavity and a sample loaded cavity. From the quality factors (Figure 2.9(b)) and the difference between the two resonant frequencies (empty cavity and thin film loaded cavity) the dielectric constant of the thin film is calculated. The dimensions of the cavity determine the frequency for which the dielectric constant is calculated. This method is very helpful for precise calculation of dielectric constant of thin film. But this method is not suitable for broadband frequency measurement.

2.5.1 Coplanar Waveguide (CPW)

Coplanar Waveguide is a kind of planar transmission line and was invented by Cheng P. Wen in 1969 [43]. A conventional CPW consists of a center conductor that carries the RF signal and is sandwiched between a pair of ground conductors, as shown in the Figure 2.10. The cut-off frequency of the CPW transmission line is given by the width (s) of the signal conductor, gap (g) between the signal and the ground lines and the dielectric constant of the substrate on which CPW is fabricated (Figure 2.11) [44].

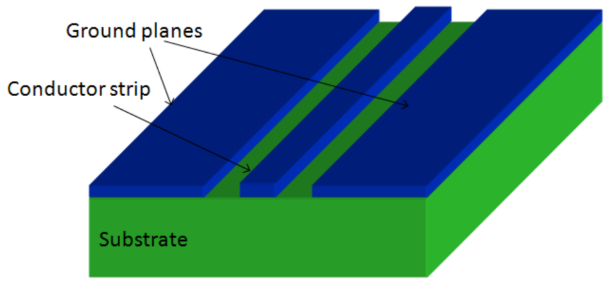

Figure 2.10: Coplanar waveguide structure

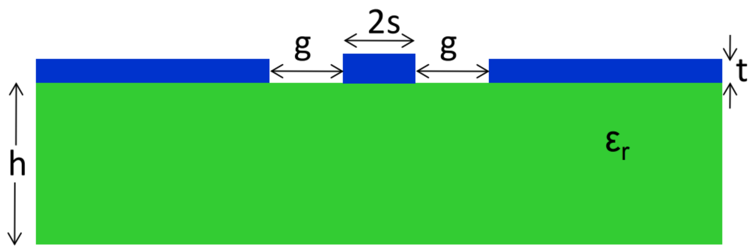

Figure 2.11: Cross-sectional view of a CPW

2.5.1.1 Quasi-static Analysis by Conformal Mapping Technique

CPW structure does not support the TEM (Transverse Electromagnetic) mode. In TEM mode both Electric and Magnetic fields are transverse (perpendicular) to the direction of propagation. That means, there are nonzero electric and magnetic field components along the propagation direction for an electromagnetic wave propagating through the CPW. These modes are known as quasi-TEM modes (hybrid modes) which are good enough to represent characteristic properties of a CPW. The cross-sectional view of a CPW is shown in Figure 2.11. The center strip has width of 2s, the gap between center strip & ground plane is g and the dielectric constant of the substrate is ϵ_0. Now with the help of conformal mapping technique an analytical expression can be derived for effective dielectric constant of the RF mode and characteristic impedance of the transmission line [45]. In the current analysis, ground planes are assumed to have infinite width and all the conductors are assumed to have a zero thickness.

The analytical equation is based on partial capacitance technique [46]. The effective dielectric constant and characteristics impedance of such a structure (Figure 2.11) can be expressed by Equation 2.29 and 2.30 respectively [47].

$$\epsilon_{eff} = 1 + q_1(\epsilon_r - 1) \tag{2.29}$$

$$Z_C = \frac{30\pi}{\sqrt{\epsilon_{eff}}} \frac{K(k_0^{'})}{K(k_0)} \tag{2.30}$$

q_1 is called the filling factor (Equation 2.31) and K is the complete elliptical integral of the first kind (Equation 2.32).

$$q_1 = \frac{1}{2} \frac{K(k_1)}{K(k_1^{'})} \frac{K(k_0^{'})}{K(k_0)} \tag{2.31}$$

$$K(k) = \int_0^{\pi/2} \frac{d\theta}{\sqrt{1 - k^2 sin^2\theta}} \tag{2.32}$$

The factors k_0, $k_0^{'}$, k_1 and $k_1^{'}$ are given by Equation 2.33, 2.34, 2.35 and 2.36 respectively.

$$k_0 = \frac{s}{s+g} \tag{2.33}$$

$$k_0^{'} = \sqrt{1 - k_0^2} \tag{2.34}$$

$$k_1 = \frac{sinh\left(\frac{s\pi}{2h}\right)}{sinh\left(\frac{\pi(s+g)}{2h}\right)} \tag{2.35}$$

$$k_1^{'} = \sqrt{1 - k_1^2} \tag{2.36}$$

2.5.1.2 Coplanar Waveguide with Multilayer Substrate

In order to find the dielectric constant of thin film of high-κ dielectric deposited on a substrate, it is important to extend the conformal mapping technique to a multi layer substrate. The cross-sectional view of a CPW structure of with multilayer dielectric is shown in Figure 2.12.

In Figure 2.12 the layers with dielectric constant ϵ_1 and ϵ_2 can be considered as the thin film of high-κ dielectric material and the substrate respectively. The effective permittivity of such CPW structure is given by [47],

$$\epsilon_{eff} = 1 + q_1(\epsilon_1 - \epsilon_2) + q_2(\epsilon_2 - 1) \tag{2.37}$$

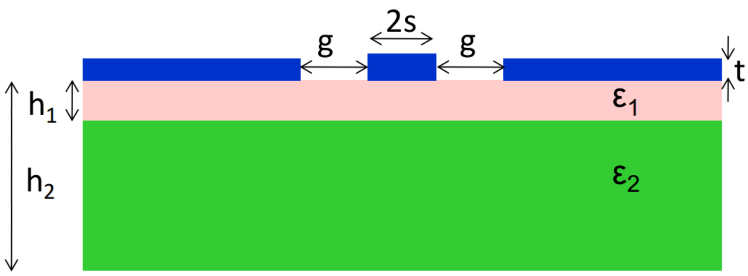

Figure 2.12: Cross-sectional view of a multilayer substrate CPW

Where the filling factors, q_i and the factors k_i & $k_i^{'}$ are,

$$q_i = \frac{1}{2}\frac{K(k_i)}{K(k_i^{'})}\frac{K(k_0^{'})}{K(k_0)} \tag{2.38}$$

$$k_i = \frac{sinh\left(\dfrac{s\pi}{2h_i}\right)}{sinh\left(\dfrac{\pi(s+g)}{2h_i}\right)} \tag{2.39}$$

$$k_i^{'} = \sqrt{1-k_i^2} \tag{2.40}$$

If the substrate consists of n different layers then the equation will be,

$$\epsilon_{eff} = 1 + \sum_{i=1}^{n} q_i(\epsilon_i - \epsilon_{i+1}) \tag{2.41}$$

2.5.2 Effective Dielectric Constant from S-parameters

The analytical expression of the effective dielectric constant of CPW as explained ion the Section 2.5.1 when compared with the measured effective dielectric constant of the fabricated CPW gives the dielectric constant of the high-κ dielectric thin film. The following section elucidates the procedure to calculate the ϵ_{eff} of a coplanar waveguide transmission line from a broadband S-parameter measurement.

At first the S-parameters are converted to ABCD matrix. When the coplanar waveguide is represented by a two port system and tested in a controlled microwave system ($Z_0 = 50\ \Omega$) then the relationship between S-parameters and ABCD matrix can be expressed by [48],

$$A = \frac{1 + S_{11} - S_{22} - \Delta S}{2S_{21}} \tag{2.42}$$

$$B = \frac{(1 + S_{11} + S_{22} + \Delta S)Z_0}{2S_{21}} \tag{2.43}$$

$$C = \frac{(1 - S_{11} - S_{22} + \Delta S)}{2S_{21}Z_0} \tag{2.44}$$

$$D = \frac{(1 - S_{11} + S_{22} - \Delta S)}{2S_{21}} \tag{2.45}$$

where,

$$\Delta S = S_{11}S_{22} - S_{21}S_{12} \tag{2.46}$$

Again, the ABCD matrix can be expressed in terms of complex propagation constant, γ and the characteristic impedance of the coplanar waveguide, Z_C. The ABCD matrix of a coplanar waveguide having a length l is [48],

$$\begin{bmatrix} A & B \\ C & D \end{bmatrix} = \begin{bmatrix} cosh(\gamma l) & Z_C sinh(\gamma l) \\ \dfrac{sinh(\gamma l)}{Z_C} & cosh(\gamma l) \end{bmatrix} \tag{2.47}$$

When Equations 2.42 - 2.47 are combined the expression for complex propagation constant can be found,

$$e^{-\gamma l} = \left\{ \frac{1 - S_{11}^2 + S_{21}^2}{2S_{21}} \pm X \right\}^{-1} \tag{2.48}$$

where,

$$X = \left\{ \frac{(S_{11}^2 - S_{21}^2 + 1)^2 - (2S_{11})^2}{2S_{21}^2} \right\}^{\frac{1}{2}} \tag{2.49}$$

The real and the imaginary terms of the complex propagation constant, γ are known as the attenuation constant, α and the phase constant, β. Then the phase constant is used to express the effective dielectric constant.

$$\gamma = \alpha + j\beta \tag{2.50}$$

$$\beta = \frac{2\pi}{\lambda}\sqrt{\epsilon_{eff}} \tag{2.51}$$

If the dielectric permitivitty of the substrate is known then the dielectric permitivitty of the high-κ dielectric thin film can be determined using the Equations 2.41 and 2.51.

2.5.3 Dielectric Loss

The total loss of the coplanar waveguide can also be estimated from the S-parameters. An estimation of the total loss of a CPW can be extracted from the real part (α) of the complex propagation constant, γ.

The coplanar waveguide has different types of losses. The most three important losses are the conductor loss, the dielectric loss and the radiation loss.

$$\alpha = \alpha_C + \alpha_D + \alpha_R \tag{2.52}$$

Normally, the radiation loss is dominant over 200 GHz of an RF signal. So the radiation loss, α_R is considered to be zero. So the total loss becomes,

$$\alpha = \alpha_C + \alpha_D \tag{2.53}$$

The conductor loss, α_C is expressed by [49] Equation 2.54 (in dB/m).

$$\alpha_C = 8.68 \frac{R_s b^2}{16 Z_C K^2(k)(b^2 - a^2)} \left(\frac{1}{a} ln\left(\frac{2a}{\Delta} \frac{b-a}{b+a} \right) + \frac{1}{b} ln\left(\frac{2b}{\Delta} \frac{b-a}{b+a} \right) \right) \tag{2.54}$$

Here, a, b & Δ are defined as,

$$a = s \tag{2.55}$$

$$b = s + g \tag{2.56}$$

$$\Delta = \frac{t}{4\pi e^{\pi}} \tag{2.57}$$

R_s is the surface resistance of the metal. If the conductivity of the metal is σ_C then,

$$R_s = \frac{1}{\delta \sigma_C} \tag{2.58}$$

δ is the skin depth of the metal which is expressed by,

$$\delta = \sqrt{\frac{2}{\omega \mu_0 \sigma_C}} \tag{2.59}$$

After the calculation of α_C the dielectric loss, α_D can be easily calculated from Equation 2.53. This gives the effective loss tangent (in dB/cm).

$$\alpha_D = 0.91 \sqrt{\epsilon_{eff}} f(GHz) tan\delta_{eff} \tag{2.60}$$

If the losses from the substrate layers are neglected then the loss tangent of the high-κ dielectric thin film can be measured using Equation 2.61 [49]. If the layer-1 of Figure 2.12 is considered as the high-κ dielectric thin film then the loss tangent of the high-κ thin film will be,

$$tan\delta_1 = \frac{\epsilon_{eff} tan\delta_{eff}}{q_1 \epsilon_1} \tag{2.61}$$

Chapter 3

Deposition and Characterization of High-κ Material Thin Film

In this chapter, the deposition technique of high-κ thin film and its characterization is discussed. In current thesis, the use of BTO was investigates as a high-κ dielectric material for the CC-SOH. The dielectric constant of sputtered BTO thin film is ~30 in the microwave frequencies [50]. The dielectric constant of BTO thin films in the microwave frequencies are even higher which are grown epitaxially (~500) [51]. In Section 3.1, the deposition technique of BTO and post deposition annealing process is explained. The optical and the RF characteristics of these thin films are analyzed in Section 3.2.

3.1 Deposition of $BaTiO_3$ (BTO)

There are a number of techniques to deposit thin films. Some of the deposition techniques are mentioned in Section 2.4.1. We are mainly relying on a physical thin film deposition technique - RF magnetron sputtering. As mentioned in the previous chapter, BTO has been selected as the high-κ dielectric material. In this section, the BTO thin film deposition procedure will be discussed.

The BTO thin films are deposited by RF magnetron sputtering on two different substrates - silicon substrates and silicon substrates with 2 μm thermal oxide. The sputtering facility of the Institute of Nanotechnology (INT) of Karlsruhe Institute of Technology (KIT) is used for the depositions.

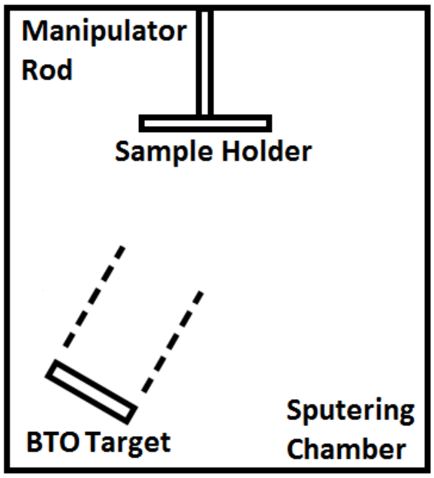

Figure 3.1: Schematic diagram of the sputtering setup

A deposition rate of 320 nm/hr is determined for the sputtered film. The film thickness varied within ± 50 nm of the mean thickness across the length of the 40 mm $\times$ 40 mm sample. However, the uniformity of the deposited film can be improved by employing sample rotation during sputtering. But, in order to fabricate CC-SOH devices, the BTO films are needed to be lifted-off using a PMMA mask. Sample rotation in this case results in unwanted sidewall depositions that make the lift-off process difficult. Hence, in order to keep the process consistent, the samples are always deposited with no smaple rotation. Instead rotating the sample holder the manipulator rod of the sputtering chamber is adjusted to get a better uniformity of the BTO film (Figure 3.2). The BTO films are always deposited at a constant RF power of 100 W. The base pressure is $\sim 1.7 \times 10^{-8}$ mbar and the working pressure is $\sim 5 \times 10^{-3}$ mbar. The sputtering was done in presence of Ar with a flowrate of 30 sccm.

The presence of O_2 during BTO sputtering helps maintaining the stoichiometry of BTO thin film. Since the BTO is sputtered in absence of O_2 the thin films are stoichiometrically different. Moreover, high substrate temperature was avoided due to the presence of PMMA on the actual devices. As a result, the sputtered BTO thin films are amorphous in nature. The thin films deposited in this way has a low dielectric constant and high dielectric loss. So post-deposition annealing is done to crystallize the amorphous film. The environment is in O_2 in order to also compensate the stoichiometry.

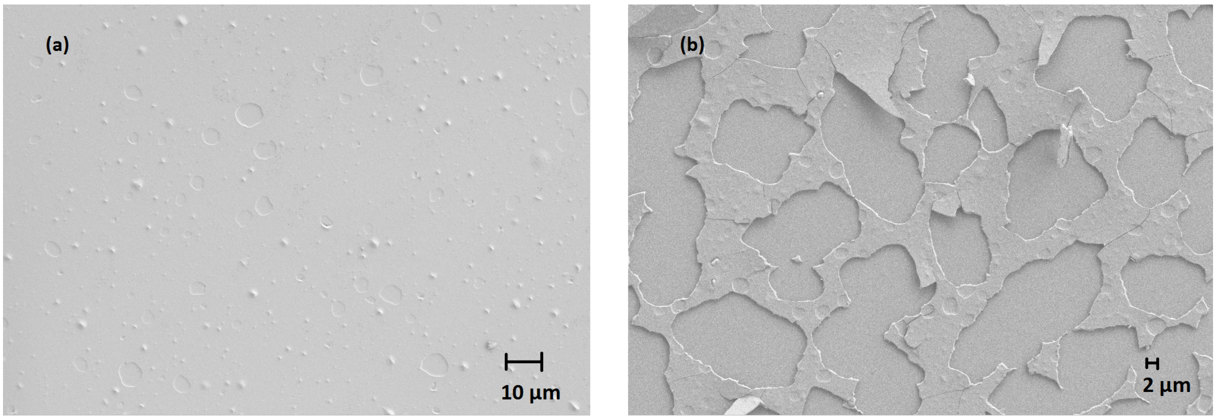

Figure 3.2: 650 nm BTO thin film (a) as deposited and (b) after annealing at 650 °C for 2 hours with temperature ramp down rate of 31.25 °C/min

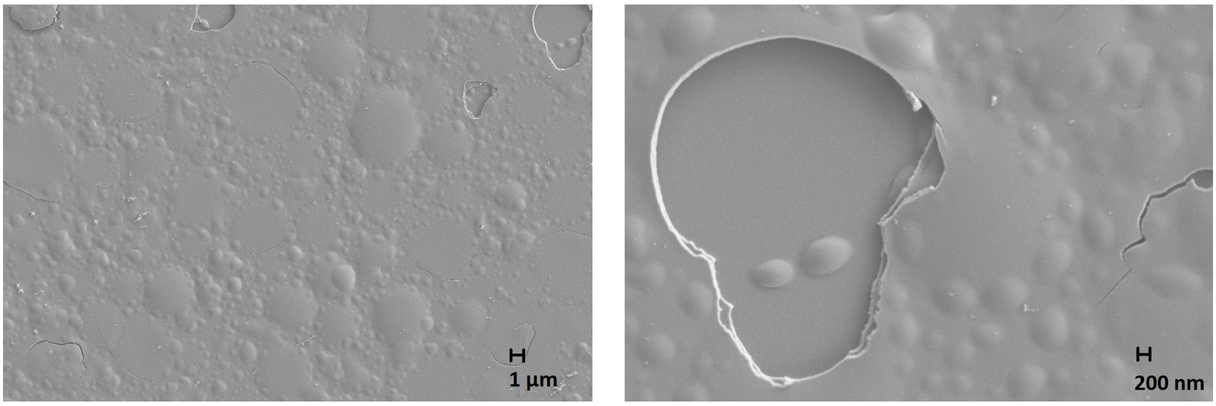

Figure 3.3: 650 nm BTO thin film after annealing at 550 °C for 20 mins with temperature ramp down rate of 2.5 °C/min

The BTO thin film shows polycrystallinity after annealing at a temperature of 650 °C [52]. During the initial tests, 650 nm thick BTO thin that were films deposited on Si substrates were annealed at 650 °C for 2 hrs with ramp down rate of 31.25 °C/min. As can be seen in the Figure 3.1(b), the film cracked (Figure 3.2(b)) due to the high thermal expansion coefficient mismatch between BTO and Si [53]. BTO ($\sim 10{\times}10^{-6}$ K^{-1}) has almost five times higher thermal expansion coefficient than that of Si (2.6×10^{-6} K^{-1}). For subsequent annealing procedures, the annealing temperature, the annealing time and the temperature ramp down rate were reduced to 550 °C, 20 mins and 2.5 °C/min respectively. This improved the annealing process but could not avoid the cracking of the film (Figure 3.3).

In order to ease the stress in the films during annealing, Si substrates with 2 μm SiO2

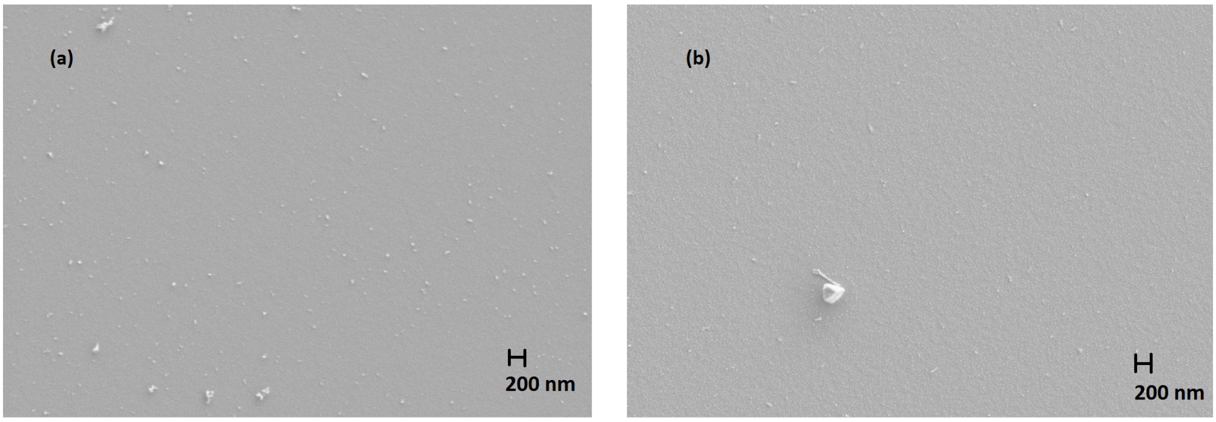

Figure 3.4: 650 nm BTO thin film (a) as deposited and (b) after annealing at 650 °C for 20 mins with temperature ramp down rate of 2.5 °C/min

on top are used for further experiments. SiO_2 has a higher thermal expansion coefficient (5.6 $\times 10^{-6}$ k^{-1}) than that of Si which is almost half of the thermal expansion coefficient of BTO. As can be seen in the Figure 3.4 (b), a 300 nm BTO film after annealing for about 20 min at 650 °C (ramp down rate of 2.5 °C/min) did not show any cracks in the thin film asserting the fact that the stress in the film is greatly reduced. So later on, BTO thin films were always deposited on Si substrates passivated with thick SiO_2 for thin film characterization purpose.

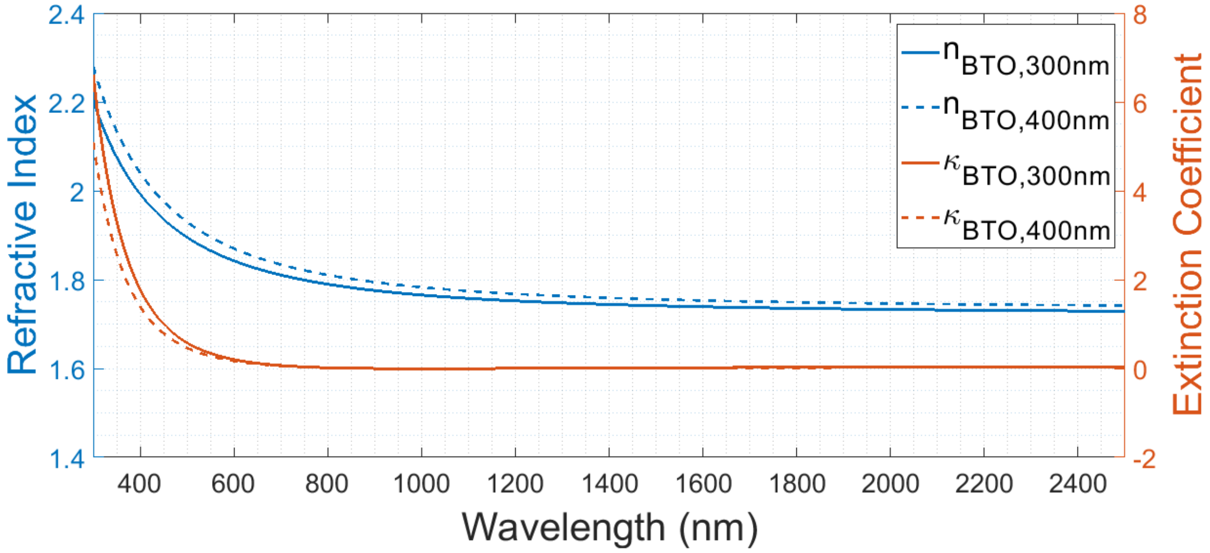

Figure 3.5: Refractive index & extinction coefficient curves for BTO thin films)

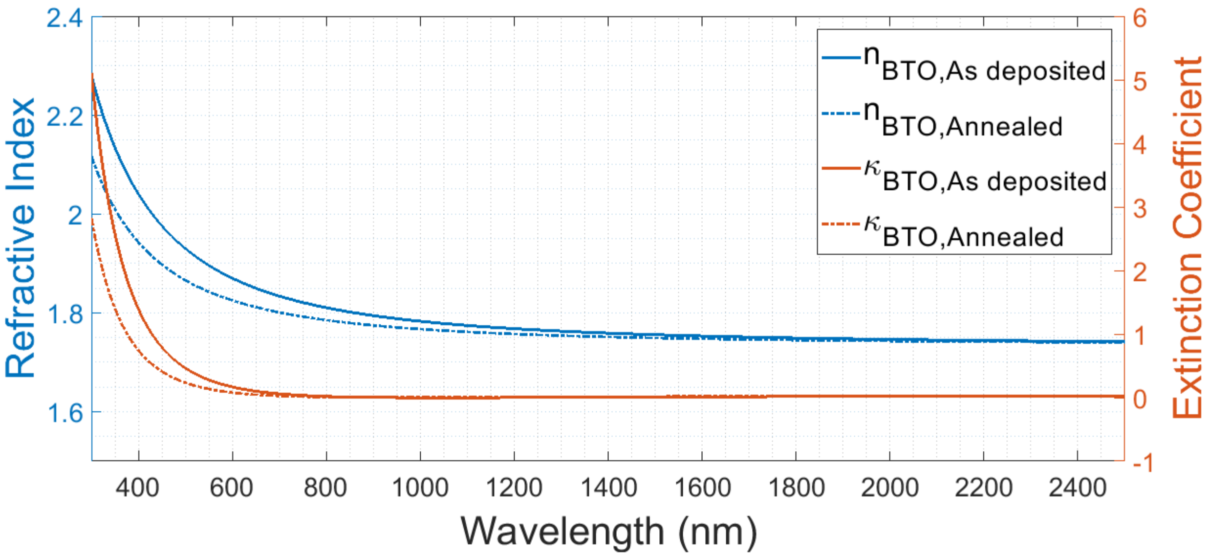

Figure 3.6: Refractive index & extinction coefficient curves for BTO (before and after annealing process)

3.2 Characterization of High-κ Thin Film

The optical and electrical properties of thin films often vary from bulk materials. Additionally, the properties of the dielectric thin films depend upon the thickness, deposition technique and the deposition parameters. In this section different characteristics of our sputter deposited BTO thin films will be presented.

3.2.1 Optical Characterization

The complex refractive indices (optical characteristics) of the thin films were measured in the cleanroom of the Institute of Microstructure Technology (IMT) of KIT using a SENTECH SE850 Ellipsometer. The procedure of determining the refractive index from the data (amplitude component, Ψ and the phase difference, Δ) measured by an ellipsometer is explained in Appendix A. The ellipsometer can measure the Ψ and Δ values for a wavelength range of 285-850 nm. To get the Ψ and Δ values for higher wavelengths (850-1700 nm) an Agilent Cary 640 FTIR Spectrometer was integrated to the setup. So we have the refractive indices and extinction coefficients of the thin films for a very broad optical frequency range.

For BTO the complex refractive index measurement was carried out for thin films of two different thicknesses (300 nm & 400 nm) which were deposited by sputtering on 2 μm SiO_2/Si substrates. The refractive index and the extinction coefficient curves are shown in Figure 3.5. The refractive index of the 400 nm thick BTO thin film has slightly higher refractive index than that of BTO thin film of 300 nm thickness. But the extinction coefficients of both films are almost the same. The refractive indices of the thin films (300 nm 400 nm) at a wavelength of 1550 nm are approximately 1.74 1.754 respectively. The extinction coefficient of both the thin films is around 0.011 at 1550 nm wavelength. Later these values were used to design the slot waveguides of CC-SOH modulators (Section 4.1.1).

The complex refractive index measurement was also carried out for an annealed BTO thin films. Figure 3.6 shows that, the refractive index and the extinction coefficient were almost unchanged after the post deposition annealing of BTO. Both the as deposited and the annealed thin films shown in Figure 3.6 have a BTO thickness of 400 nm.

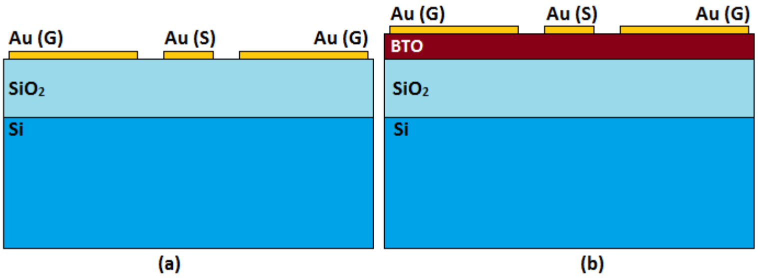

Figure 3.7: Coplanar waveguide structure (a) on bare substrate (optimized to 50 Ω) and (b) the BTO thin film

3.2.2 RF Characterization

The BTO thin films were also characterized in the RF regime. As described in Section 2.5, for the RF characterization (complex dielectric constant) of the BTO thin films for a broad RF microwave frequency range (0-65 GHz) coplanar waveguide structures need to be fabricated on the BTO thin films. The S-parameters of the coplanar waveguides fabricated on BTO thin films on Si substrates passivated with 2 μm SiO_2 substrates are measured. From the S-parameters the complex permittivity of BTO is determined. Normally, if the width of the ground electrode is more than or equal to the width of center (signal) electrode then the coplanar waveguide can be considered as a conventional coplanar waveguide (with infinite ground width) [54]. So the ground electrode width was always kept at least 5 times of the center electrode. The metal (Au) thickness of the coplanar waveguide is around 150 nm and hence the effect of the metal thickness can be ignored in the calculation of the dielectric constant. But it has to be considered in order to accurately calculate the dielectric loss (Section 2.5.3). Reference structures with 50 Ω impedance are designed on 2 μm SiO_2 on Si using commercially available software CST MWS. The same coplanar waveguide geometry is fabricated also on BTO thin films so that the influence of unknown quantities (dielectric constant of substrate etc.) is eliminated by referencing. The cross-section of the coplanar waveguides on both the bare substrate and the BTO thin film are shown in Figure 3.7.

Coplanar waveguides of different lengths were fabricated on both as deposited and annealed BTO thin films (both having a thickness of 300 nm). The extracted dielectric constant curves are shown in Figure 3.8. From Figure 3.8 it can be decided that, the dielectric constant of the annealed film is slightly better than the as deposited thin films in the higher frequency region (more than 30 GHz). For higher length of coplanar waveguides

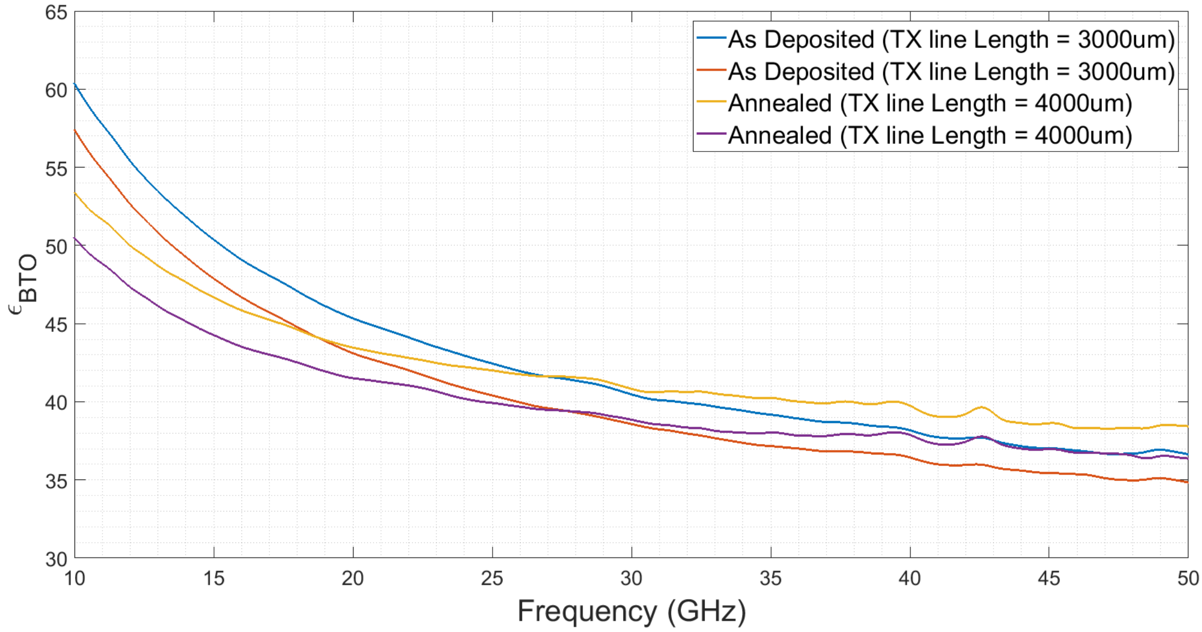

Figure 3.8: Dielectric constant curves for both as deposited an annealed thin films

the dielectric constant is always lower.

The loss tangents of same film is also extracted using the measured S-parameters. Though the dielectric constant did not improved too much after the annealing, the loss tangent showed quite an improvement. Figure 3.9 shows the loss tangents for both the as deposited and the annealed thin films.

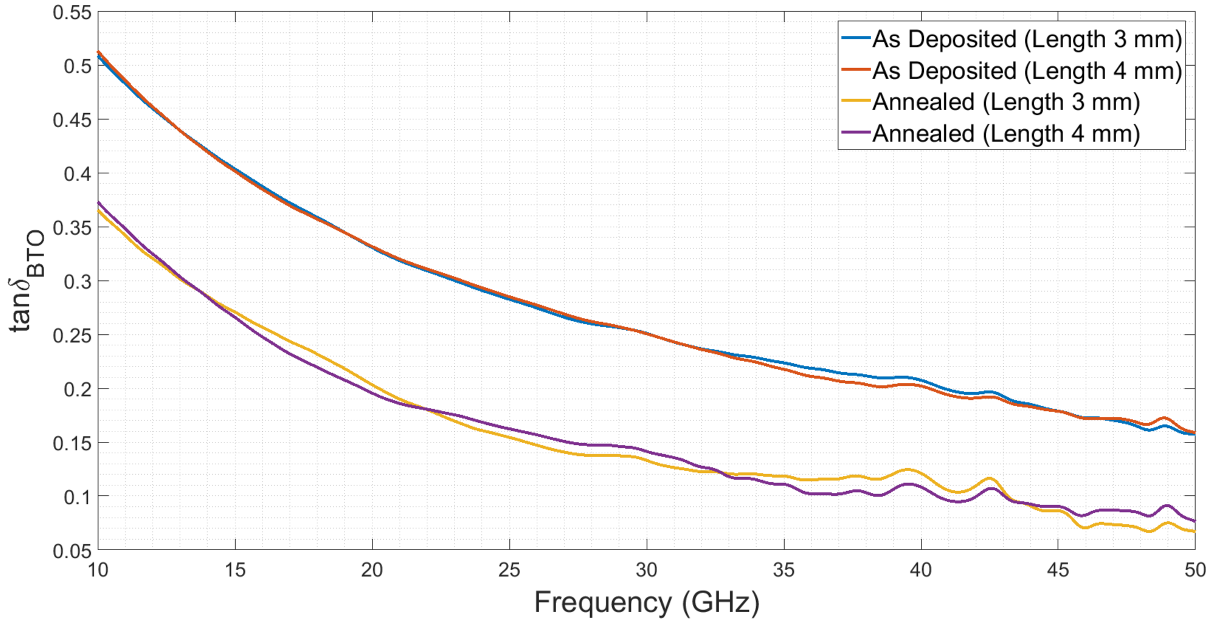

Figure 3.9: Loss tangent curves for both as deposited an annealed thin films

Chapter 4

Design and Fabrication of CC-SOH Modulators

After the characterization of the optical and RF properties of BTO thin films the CC-SOH modulators are designed and fabricated which will be discussed in this chapter. In Section 4.1, the simulations to design a CC-SOH Mach-Zehnder modulator are discussed. The fabrication steps to realize a CC-SOH modulator is outlined in Section 4.2.

4.1 Simulations

Based on the optical and RF characteristics of the BTO thin films the Mach-Zehnder modulators are designed using CST MWS. These simulations can be divided into two sections - optical simulations to design a slot waveguide structure and RF simulations in order to design a coplanar waveguide transmission line.

4.1.1 Optical Simulations

As presented in the Section 3.2.1, a refractive index of 1.74 (at 1550 nm) is considered for modeling the BTO thin films in CST. The cross-sectional schematic diagram of the Si slot waveguide is shown in Figure 4.1 (a). An EO polymer with a refractive index 1.67 fills the slot between the Si rails and BTO thin films are placed on the other side of the Si rails.

The structural parameters such as h_{BTO}, w_{BTO}, w_{rail} are varied with a fixed w_{slot} in order

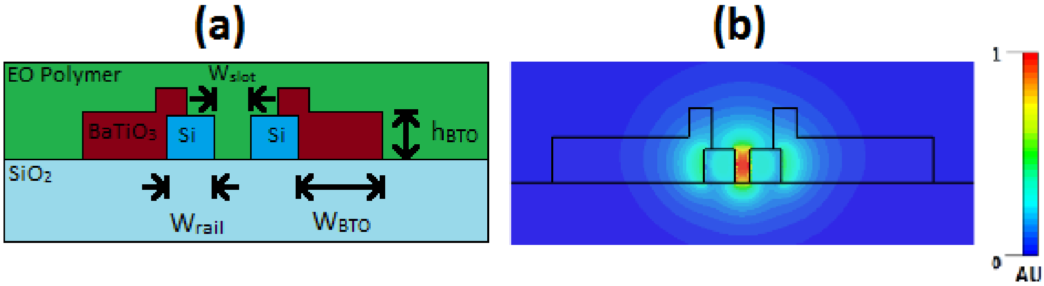

Figure 4.1: (a) Schematic diagram for Si slot waveguide design. (b) Optical field ($|E|$) distribution of a single moded Si slot waveguide with a w_{slot} = 100 nm, w_{Si} = 200 nm, w_{BTO} = 1 μm and h_{BTO} = 300 nm

to attain a single mode condition in the slot waveguide structure (Figure 4.1 (b)). The effective group refractive indices of the fundamental quasi-TE mode within the range of 1500-1600 nm wavelengths must be more than the refractive index of the outer cladding material (BTO). If the higher order modes have smaller effective group refractive indices than the refractive index of BTO then the single mode condition is fulfilled.

Sticking to a slot width, w_{slot} of 100 nm, the Si rail width, w_{Si} is optimized for single mode condition. The simulations are done for different widths (w_{BTO} = 0.5-1 μm) and thicknesses (h_{BTO} = 300-500 nm) of BTO thin films. It is observed that, the single mode (Figure 4.1 (b)) condition is always satisfied for w_{Si} in the range of 160-220 nm. Si rail width of 200 nm is chosen for the final design. Figure 4.2 shows the effective group refractive indices of the unguided higher order modes of the slot waveguide structure that are below the refractive index of BTO.

4.1.2 RF Simulations

The next step in the design of CCSOH modulator is the design of a RF transmission line. As discussed in the previous section, the w_{slot} and w_{Si} was fixed to 100 nm and 200 nm respectively. A coplanar waveguide (GSG transmission line) is designed to feed RF signal to the Mach-Zehnder modulator. Depending upon the BTO thickness (h_{BTO}) & width (w_{BTO}) the signal conductor width (w_{signal}) varies in order to design a 50 Ω GSG transmission line. The ground conductor width, w_{ground} is always kept more than five times of the signal width, w_{signal} so that the condition for a conventional coplanar waveguide with infinite ground width is fulfilled. The RF simulations are done using CST

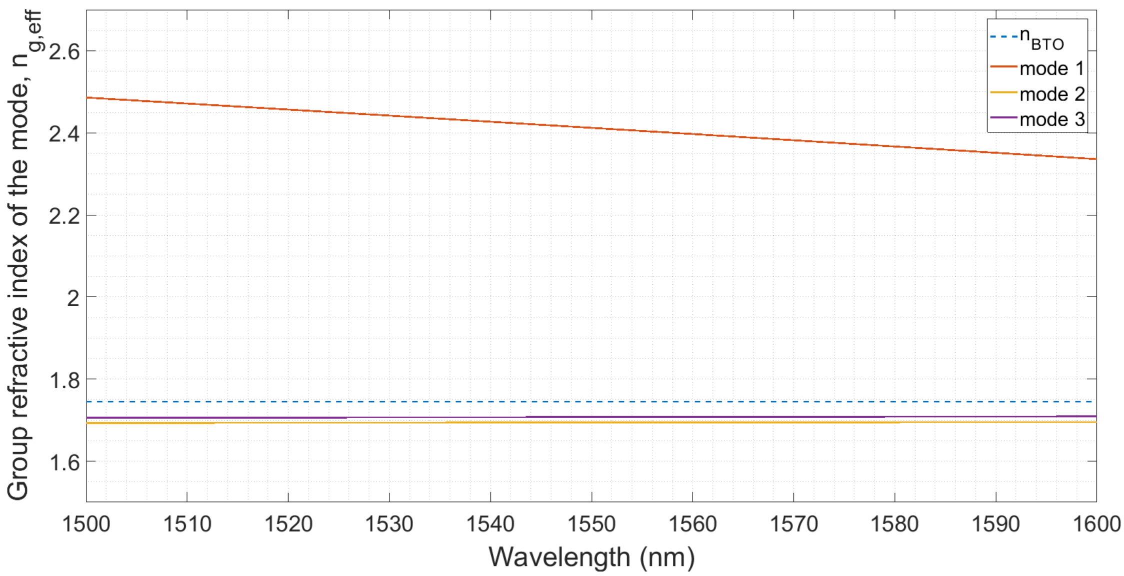

Figure 4.2: Effective group refractive index, ng,eff of different modes for a Si slot waveguide for w_{slot} = 100 nm, w_{Si} = 200 nm, w_{BTO} = 1 m and h_{BTO} = 300 nm

MWS to 50 Ω transmission lines for different BTO widths (w_{BTO}) & thicknesses (h_{BTO}). The same complex dielectric constant of BTO showed in Section 3.2.2 is used for this optimization purpose. The schematic diagram of such a structure is shown in Figure 4.3. The change of signal conductor width, w_{signal} with respect to the change of BTO width for different BTO thickness is shown in Figure 4.4 (a). The characteristic impedance, Z_C of the transmission line having $w_{BTO} = 1$ μm and $h_{BTO} = 300$ nm is shown in Figure 4.4 (b).

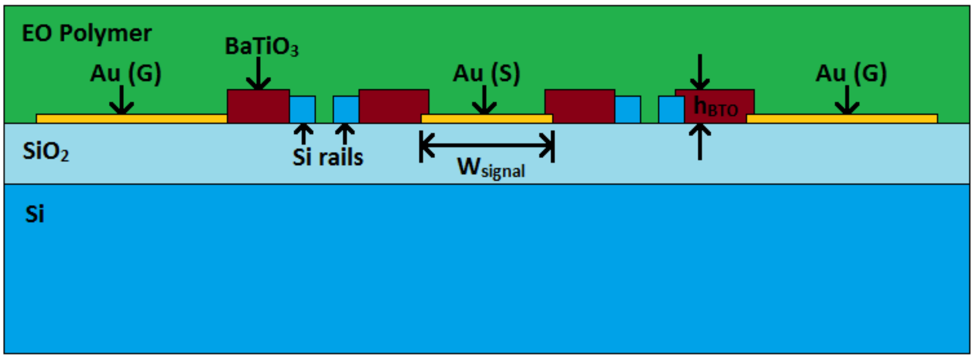

Figure 4.3: Schematic diagram for GSG transmission line optimization for 50 Ω

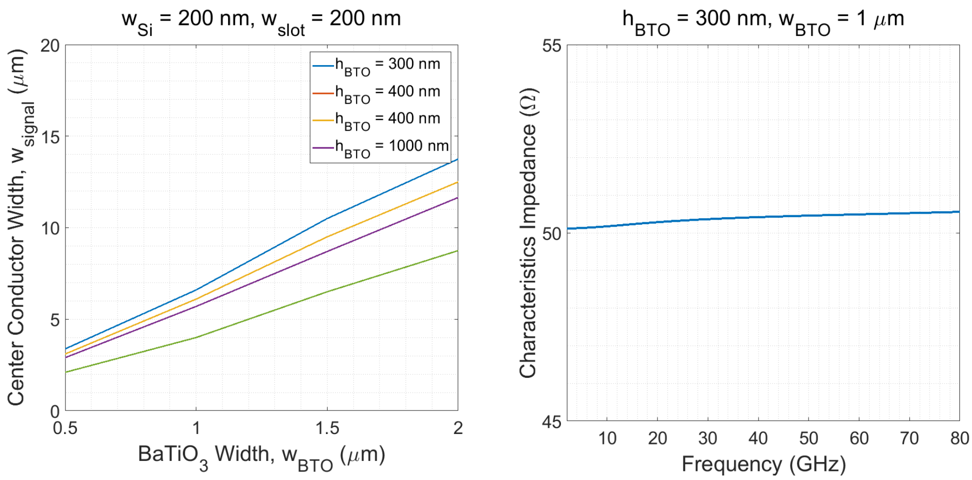

Figure 4.4: (a) Change of w_{signal} with respect to w_{BTO} for different h_{BTO} and (b) Z_c of an optimized GSG transmission line

4.2 Fabrication of CC-SOH MZM

The current sections discusses the steps required for fabrication of CC-SOH modulator.

4.2.1 Fabrication Process Flow

The fabrication process flow of the CC-SOH modulators is developed at the Institute of Microstructure Technology (IMT) and the Institute of Nanotechnology (INT) of KIT. Electron beam lithography is used for patterning the structures. The fabrication process involves 4 lithography steps and is shown in Figure 4.5. Gold structures on the corners of the chip serve as alignment markers between subsequent lithography steps. An SOI substrate having a top Si layer of 220 nm and a 2 μm thick buried oxide (SiO_2) is used. In the first lithography step, a positive tone photoresist (PMMA) is spin coated which defines the regions for partially etched grating couplers. After that, Si layer is etched partially to a depth of 70 nm by reactive ion etching (RIE). Then PMMA layer is stripped by O_2 plasma etching. In the second lithography step, a negative tone photoresist, HSQ is spincoated followed by the area definition for the Si rails of the slot waveguide. After development of HSQ in 25% TMAH solution, the top Si layer is completely etched by a Cryo etch process. In the third lithography step on PMMA mask, 150 nm thick metal layer (Au) is deposited by thermal evaporation followed by a lift-off process. A final exposure on PMMA defines the structures in which BTO thin film is sputtered between the Au electrodes and the Si rails. A final lift-off step after BTO deposition realizes a CC-SOH modulator. The thermal evaporation of Au and the sputtering of BTO are performed at INT while the rest of the fabrication processes are carried out at IMT. Thus fabricated device is ready for operation after spin coating of an EO polymer, which will be discussed in the next chapter (Chapter 5).

4.2.2 Fabricational Challenges in Sputtering

The BTO MZMs are designed for 4 different thicknesses of BTO thin films - 300 nm, 400 nm, 500 nm & 1 μm. Some fabrication challenges are faced during the sputtering of BTO. The BTO target was removed from the sputtering chamber after the deposition of thin films which was used for the characterization purpose (Section 3.1). So before sputtering the BTO thin films on the actual devices the deposition rate of the BTO sputtering is measured and the lift-off experiment of BTO is done again. Two dummy chips with MZM structures are placed on the sample holder to do the lift-off experiment and at the same time a test chip (Si substrate) is placed to measure the deposition rate (Figure 4.6). It is observed that, the deposition rate was 430 nm/hr. This is different from the previous deposition rate (320 nm/hr). The sputtering is done for 30 min (215 nm of BTO thin film). A sputtering cycle of 15 min deposition followed by 15 min pause is used to avoid deformation of PMMA mask due to excessive sample heating during the sputtering process. But the lift-off still failed which is shown in Figure 4.7.

To get a proper lift-off of BTO the film thickness is reduced. The deposition time is reduced to 5 min maintaining a pause time to 15 min for each cycle. This procedure resulted in better lift-off process as can be seen in Figure 4.8.

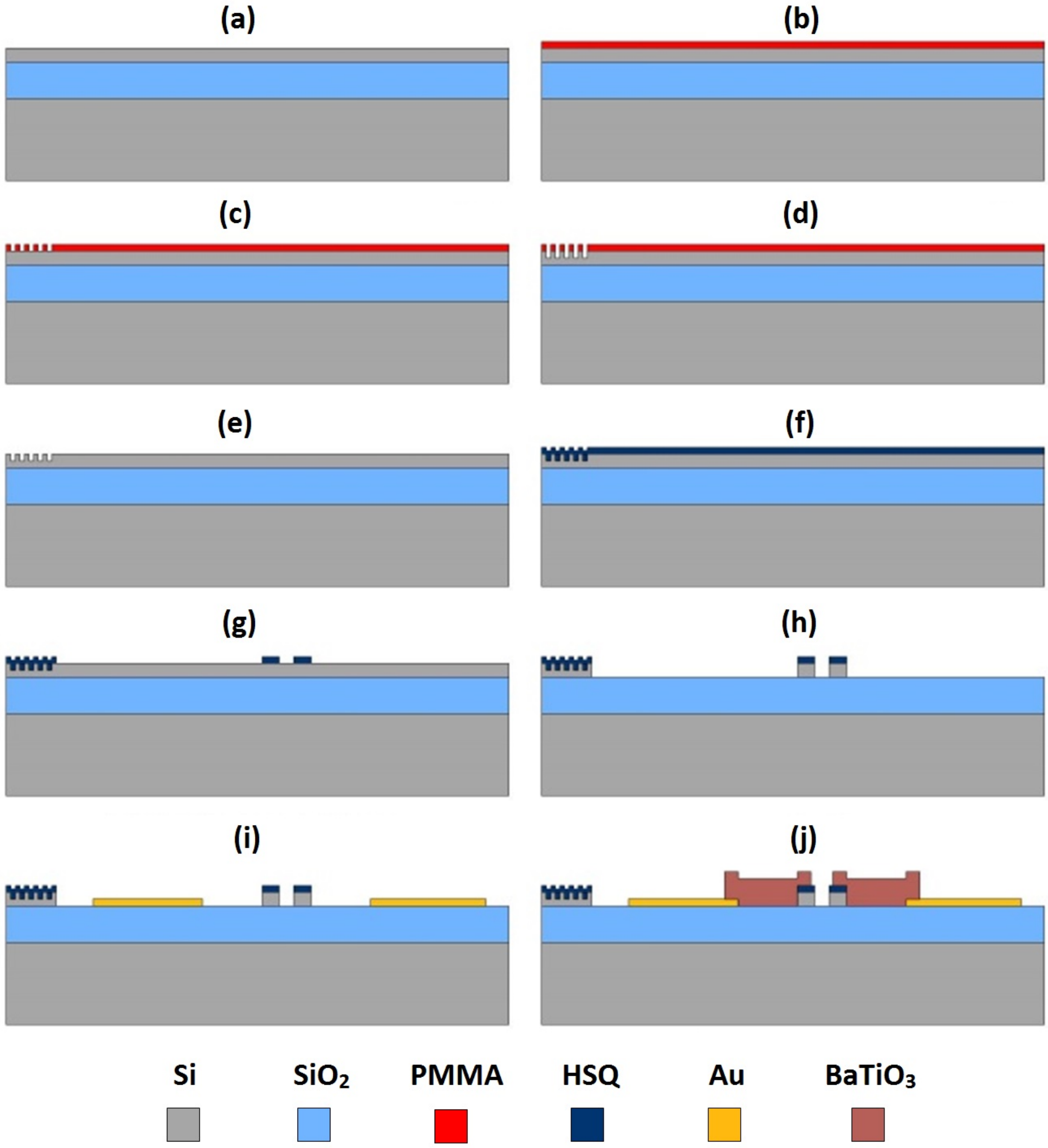

Figure 4.5: Fabrication process flow of a CC-SOH MZM with BTO as high-K dielectric. (a) SOI substrate with 220 nm thick device layer. (b) Spincoating of PMMA. (c) Definition of the region for partially etched grating coupler. (d) Partial etch of Si (70 nm) by RIE. (e) Removal of PMMA by O_2 plasma etching. (f) Spincoating of HSQ. (g) Definition of the region for Si rails of the slot waveguide. (h) Complete etch of Si by RIE. (i) Deposition of Au by thermal evaporation followed by a lift-off process. (j) Deposition of BTO by sputtering followed by a lift-off process.

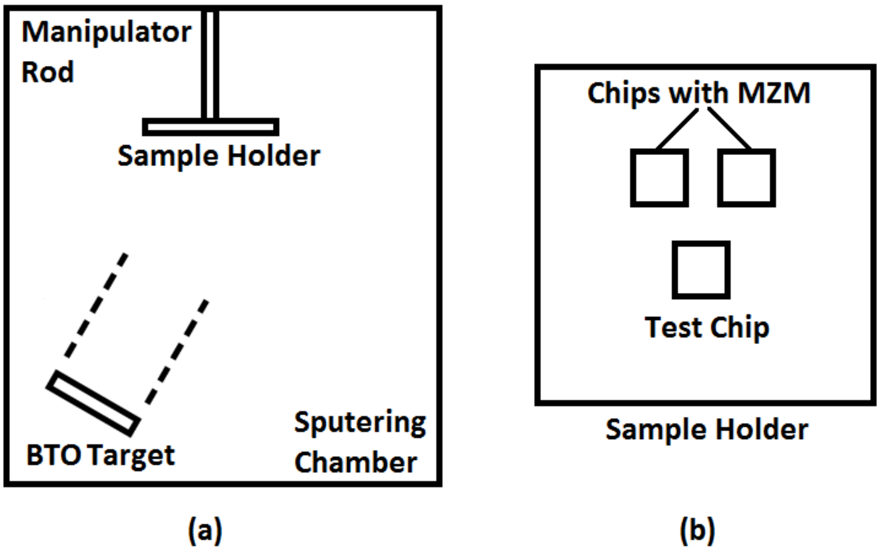

Figure 4.6: (a) Schematic diagram of the sputtering setup and (b) the arrangement of the chips on the sample holder

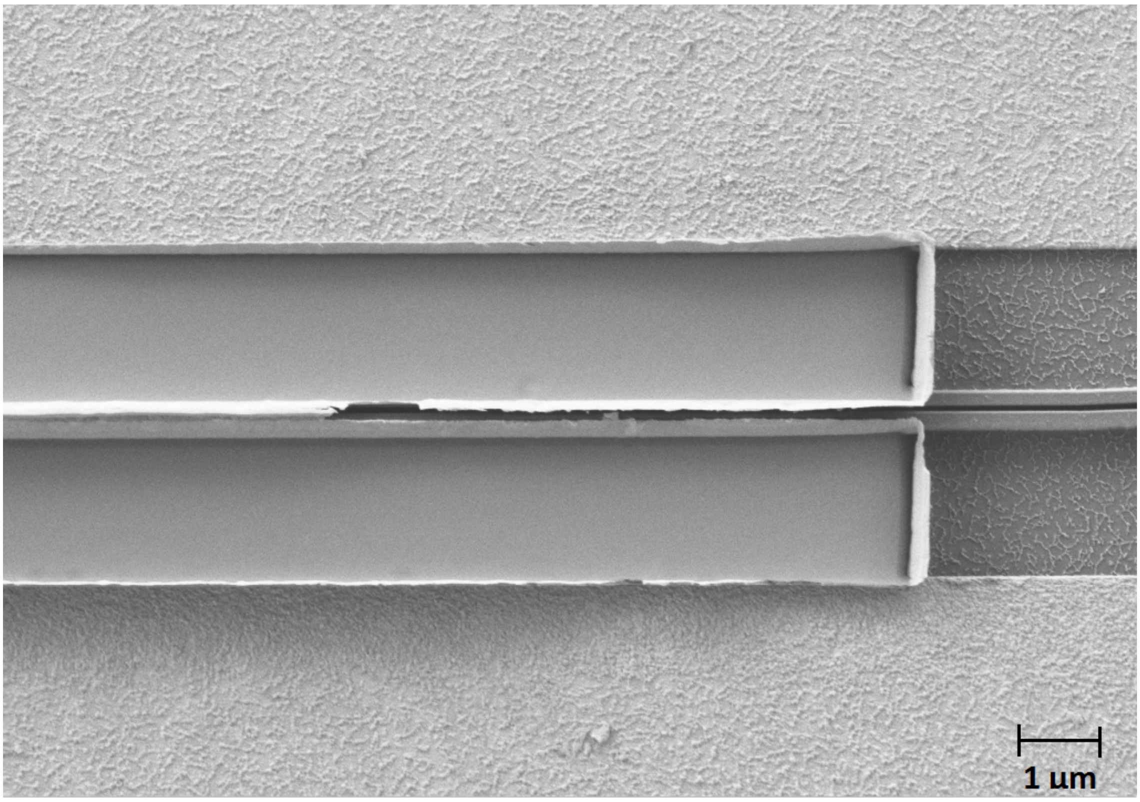

Figure 4.7: Failed strip-off of BTO

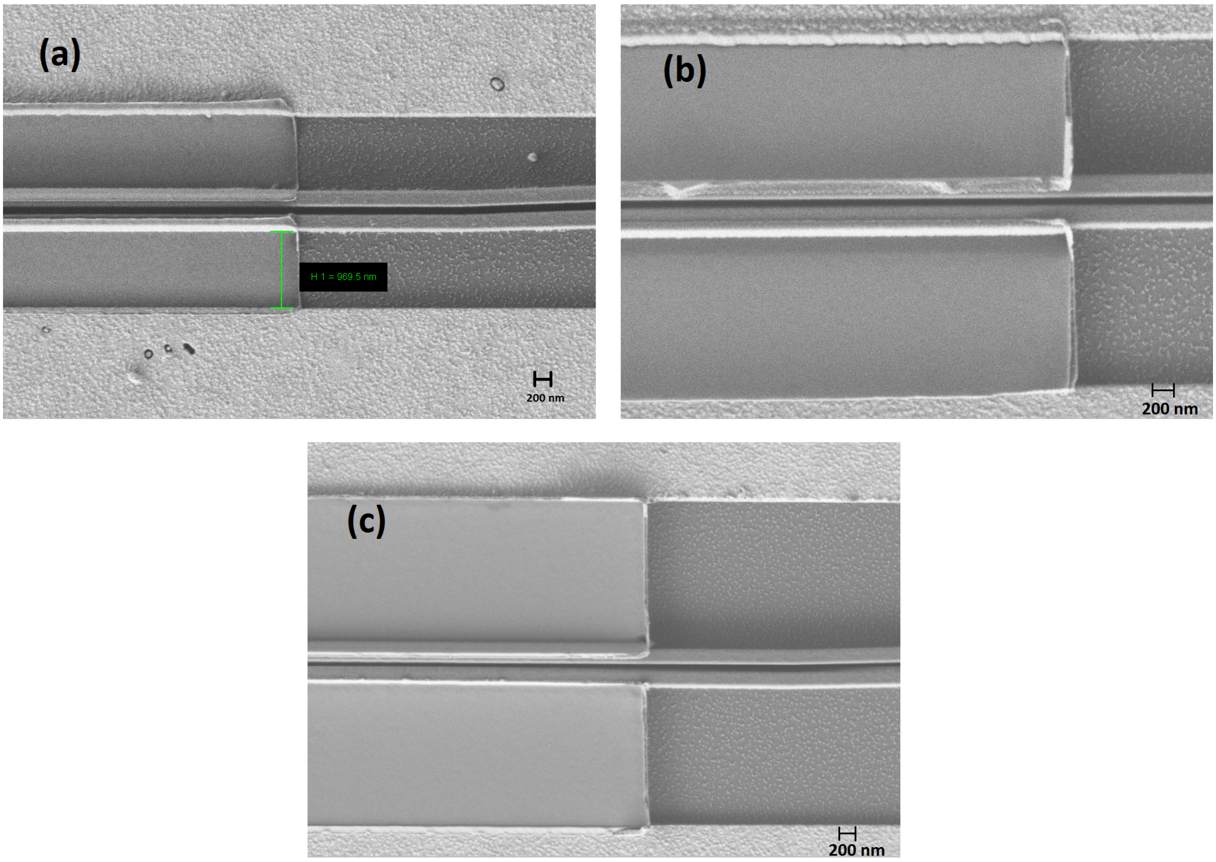

Figure 4.8: BTO MZMs having BTO thickness of (a) 50 nm, (b) 100 nm and (c) 150 nm with proper lift-off

Chapter 5

Characterization of CC-SOH Modulators

After fabrication, the CC-SOH MZMs (BTO MZMs) are characterized for transmission losses before performing modulation experiments. In Section 5.1, the measurements of optical transmissions of the BTO MZMs with different lengths and different BTO widths & thicknesses is presented. After that, the BTO MZMs went through the poling procedure which is described in Section 5.2. Finally, Section 5.3 presents the modulation bandwidth experiments of BTO MZM devices.

5.1 Optical Transmission Measurements

After the fabrication, 1 μm thick PMMA layer was spincoated on the BTO MZMs as a protective layer. The optical transmission spectra of different BTO MZMs are measured using the setup shown in Figure 5.1. The light from ANDO AQ4321A tunable laser source (TLS) is coupled to BTO MZM through an on-chip grating coupler. The polarization of the incoming light is altered using a polarzation controller to optimize the coupling efficiency of the on-chip TE grating couplers. The output signal is coupled back to a fiber using another on-chip grating coupler and the spectrum of the output optical signal is measured by an ANDO AQ6317 optical spectrum analyzer (OSA).

A false colored SEM image of a BTO MZM with a successful lift-off of BTO is shown in Figure 5.2 (a). The transmission spectra of such two modulators have been shown in

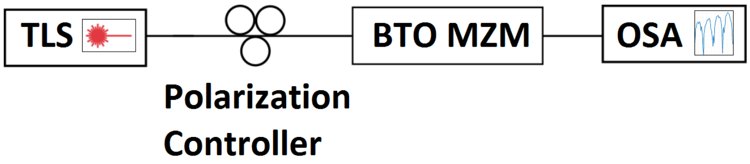

Figure 5.1: Transmission experiment setup

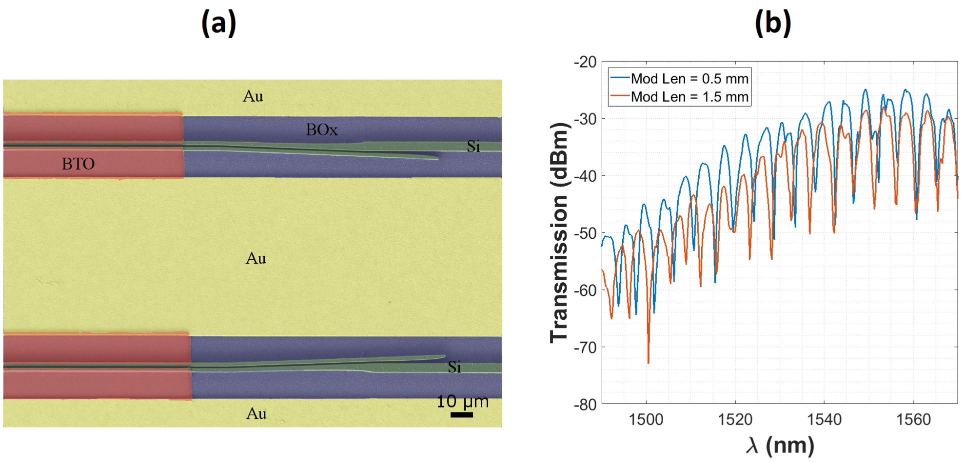

Figure 5.2: (a) SEM image of a BTO MZM with a proper lift-off. (b) Transmission spectrum of BTO MZMs of different length. The blue curve represents the transmission spectrum of the modulator BTOMZMG1 C1C B4 (Chip name: BTOMZMG1 C1C; modulator parameters: length = 0.5 mm, BTO width = 1 μm, BTO thickness = 50 nm). The red curve represents the transmission spectrum of the modulator BTOMZMG1 C1C D2 (Chip name: BTOMZMG1 C1C; modulator parameters: length = 1.5 mm, BTO width = 2 μm, BTO thickness = 50 nm).

Figure 5.2 (b). Better transmission was observed for the modulators having a shorter length.

The optical signal is carried to the modulator by strip waveguide which has a width of 500 nm. A multi-mode interference (MMI) coupler splits the light equally between the two arms of the Mach-Zehnder modulator. A strip-to-slot mode converter [55] is needed before feeding the optical signal to the modulator. After systematic measurements, the insertion losses from each of the on-chip components is evaluated. The strip waveguide and the slot waveguide have a loss of 0.7 dB/mm and 7 dB/mm respectively. The grating coupler loss is shown in Figure 5.3 (a). The measured strip-to-slot mode converter loss and the MMI loss

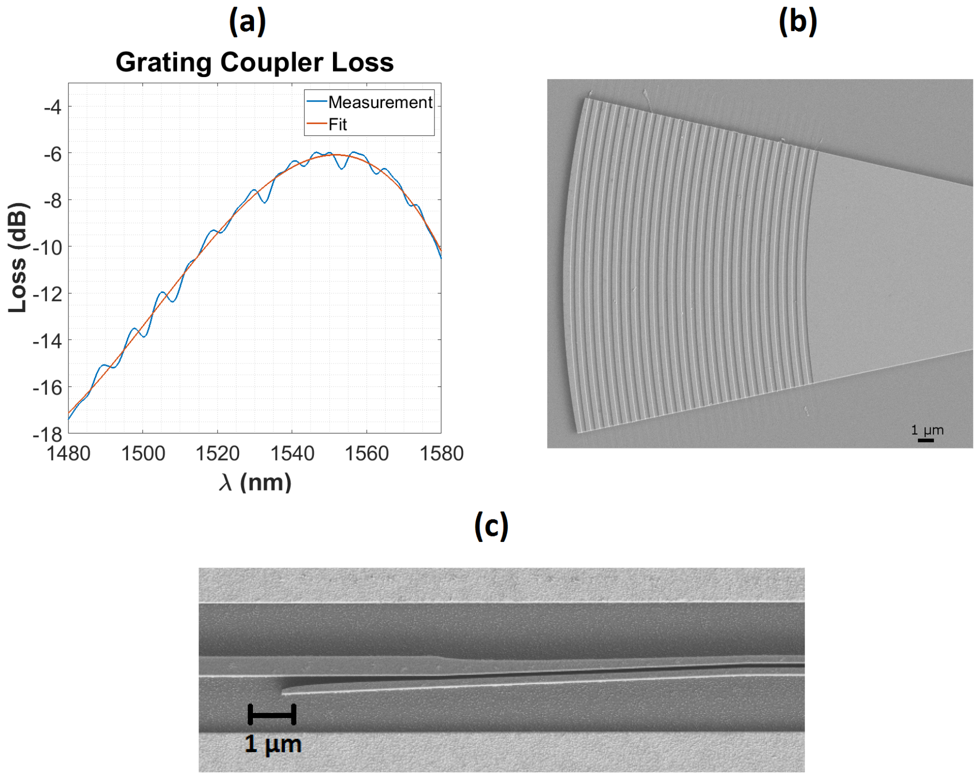

Figure 5.3: (a) Grating coupler loss. SEM images of (b) a partially etched grating coupler and (c) a strip-to-slot mode converter

at 1550 nm wavelength are 1 dB and 0.43 dB respectively. The SEM images of a partially etched grating coupler and a strip-to-slot mode converter are shown in Figure 5.3 (b) and 5.3 (c) respectively.

5.2 Poling

The electro-optic (EO) polymer is spincoated on the modulators. Yoko-2.1 is used as an EO polymer which has a glass transition temperature, T_G of 166 °C. Several MZMs are poled by 3 pin poling procedure (Figure 5.4). A poling voltage, V_{pole} of 200 V is applied on each of the arms of a BTO MZM. Two Keysight B2902A precision sources are used for applying the poling voltage. The highest voltage that can be applied by each precision source is 210 V and hence higher poling voltages could not be applied. The gap between the signal conductor and the ground conductor is 2.5 μm which gives a poling electric field of 80 V/μm. The peak poling current, I_{pole} is observed around 390 nA. The poling curves

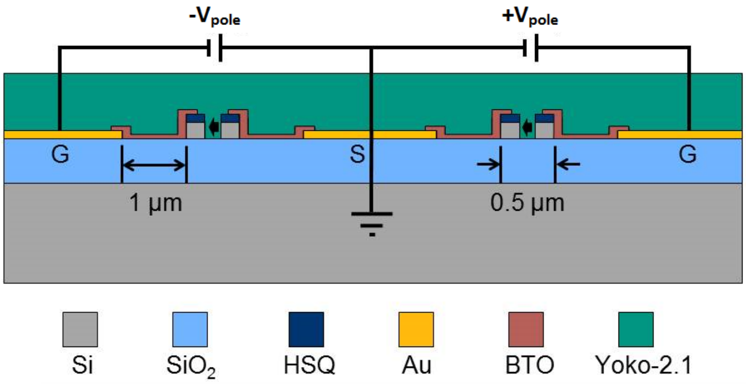

Figure 5.4: Poling of BTO MZM

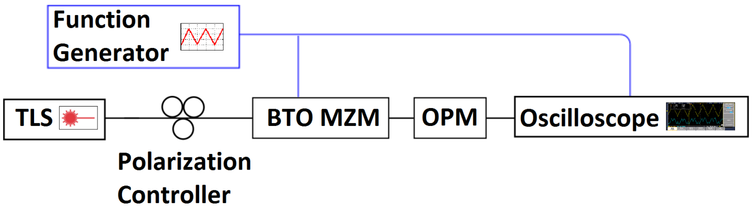

Figure 5.5: V_π measurement setup

are shown in Figure 5.6 (a).

The half-wave voltage, V_π of the poled modulators is measured using a setup shown in Figure 5.5. A tunable laser sources couples the light in and out of the BTO MZM using on-chip grating couplers. A Philips PM5133 function generator is used to generate a triangular signal having a frequency of 1 kHz and a peak to peak voltage, V_{pp} of 20 V which is applied to the BTO MZM. The modulated optical signal from the BTO MZM goes to an optical power meter (OPM). Using a digital storage oscilloscope both the input electrical signal and the modulated signal coming from the output of the OPM are observed. The V_π of the longest modulator (2 mm) measured is around 11 V (Figure 5.6 (b)) at 1543 nm. The BTO width and thickness of the modulator are 1 μm and 50 nm respectively.

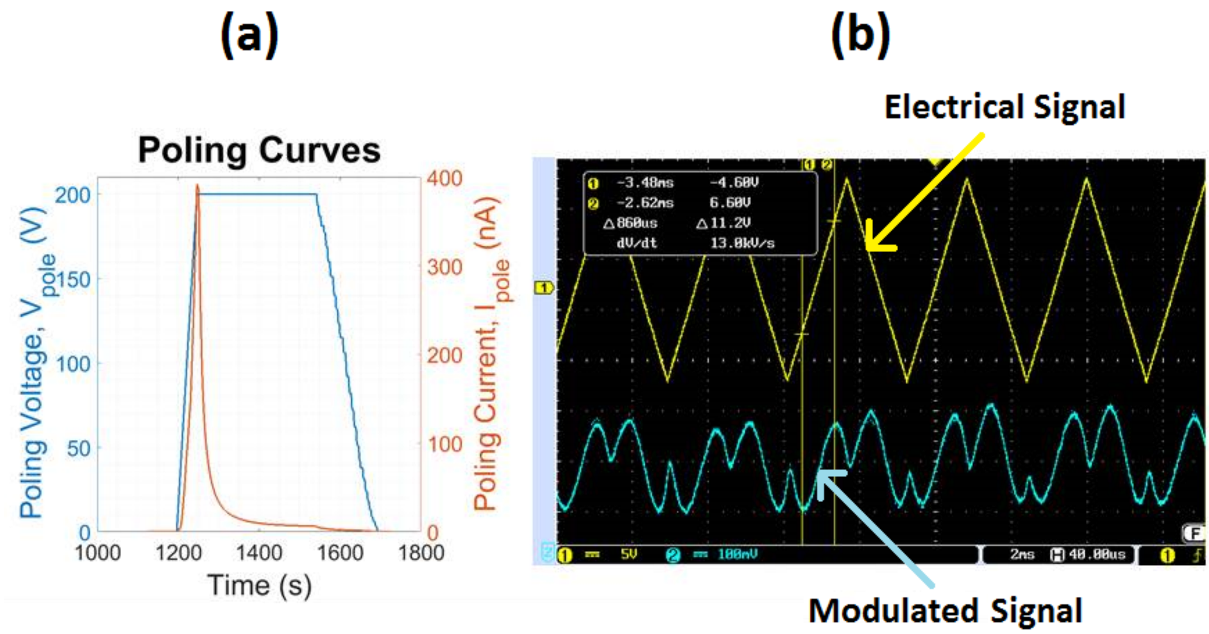

Figure 5.6: (a) Poling curves, (b) V_π measurement

5.3 Bandwidth Measurement of CC-SOH Modulator

The poled modulator is used for bandwidth measurement. A setup shown in Figure 5.7 is used for the bandwidth measurement. An Anritsu 37397C Vector Network Analyzer (VNA) is used as a source of RF signal that can generate signals from 40 MHz until 67 GHz. Since the V_π of the modulator was comparatively high, the RF signal is amplified by a Centellax UA1L65VM 3-stage broadband RF Amplifier before feeding it to the modulator. One end of the modulator is fed with an RF signal and the other end is terminated using a termination impedance, $R_t = 50\ \Omega$. The equivalent circuit is shown in Figure 5.9 (a). RF signals in the range of 5-65 GHz is applied at a 5 GHz interval. All the signals are launched from the VNA with 0 dBm power (only 60 GHz RF signal with 8 dBm and 65 GHz RF signal with 10 dBm). After amplifying with the RF amplifier the RF signals show different output power for different frequencies which is measured by a power meter (Figure 5.8). Here, it should be mentioned that, this measured power also considers the loss in the coaxial cable which connects the RF amplifier with the picoprobe. the loss in the picoprobe is considered from the datasheet provided by the supplier GGB Industries Inc. ANDO AQ4321A TLS is used to generate light at of 1547.3 nm which is coupled to the modulator through a KEOPSYS C-band Erbium Doped Fiber Amplifier (EDFA) and a polarization controller with an optical power of 18 dBm. Optical carrier signal of 1547.3

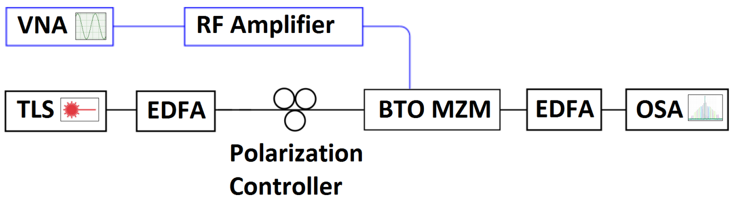

Figure 5.7: Bandwidth measurement setup

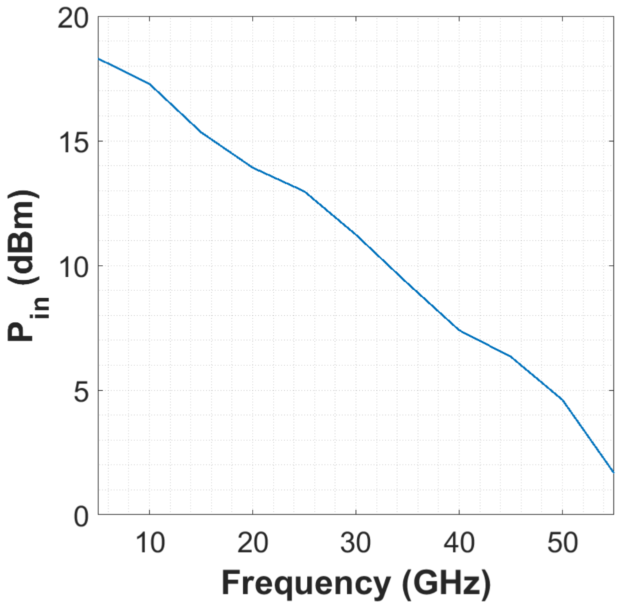

Figure 5.8: (a) Power curve after amplification of the RF amplifier

nm wavelength because of the 3 dB difference from the peak transmission power (Figure 5.1 (b)). The input power of the RF signals with higher frequencies are very low. As a result, in the higher frequency RF signals the modulated output optical signal have a very low power as well. So, the output optical signal was amplified again by a Manlight EDFA. After the amplification, the spectrum of the modulated optical signal is analyzed with an APEX AP2050 high precision Optical Spectrum Analyzer (OSA) with 20 MHz resolution.

As mentioned before, light is modulated by 5-65 GHz RF signals with an interval of 5 GHz. For each frequency there will be two modulation sidebands at $c/\lambda_{opt} \pm f_{RF}$. λ_{opt} = 1547.3 nm and f_{RF} is the frequency of the RF signals. The spectrum of all modulated output optical signals are shown in Figure 5.9 (b) where the modulation sidebands can be seen clearly until 65 GHz of RF signal. RF frequencies with higher than 65 GHz are not

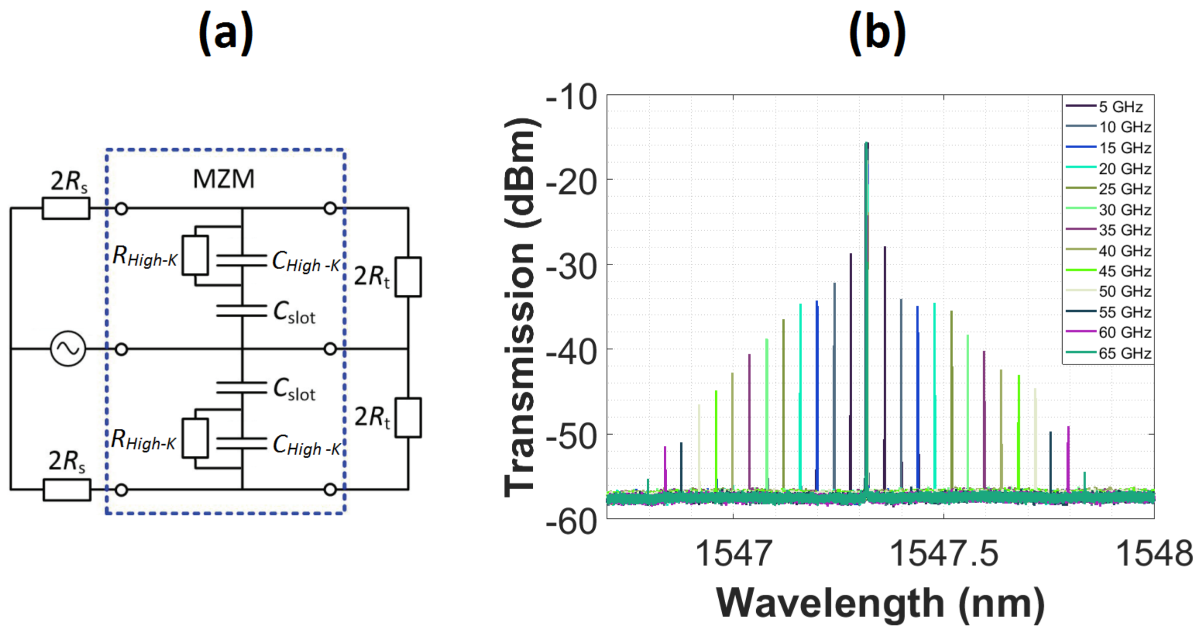

Figure 5.9: (a) Equivalent circuit of the BTO MZM, (b) Transmission spectrum of the modulated optical signal

accessible due the unavailability of the equipment.

The calculated V_π and the r_{33} using the transmission spectrum of the modulated optical signal are shown in Figure 5.10. The calculation procedure of V_π and the r_{33} are discussed in Appendix C. The V_π is approximately 13 V over the whole frequency range of the RF signal which is very close to the value (∼11 V) that was measured before. The r_{33} is around 5 pm/V which is comparatively low. Normally, for SOH devices an r_{33} of ∼90 pm/V is expected [56]. So, the poling is sub-optimal. This may happen because of insufficient poling electrical field which is around 80 V/μm. But in practice the electric field is even less. Because the voltage drop across BTO is not considered. Generally, a poling electric field of ∼110 V/μm is needed to get r_{33} of 98 pm/V [57].

Afterwards, the modulation index, m was measured using the spectrum of the modulated output optical signal which follows the square root of the input power, $\sqrt{P_{in}}$ (Figure 5.11 (a)). The calculation procedure of the modulation index is described in Appendix C. After normalization to a fixed input power (2 dBm) the modulation index becomes almost flat with respect to the frequency of the RF signal. This indicates that, the 3 dB bandwidth, f_{3dB} of the BTO MZM is higher than 65 GHz (Figure 5.11 (b)).

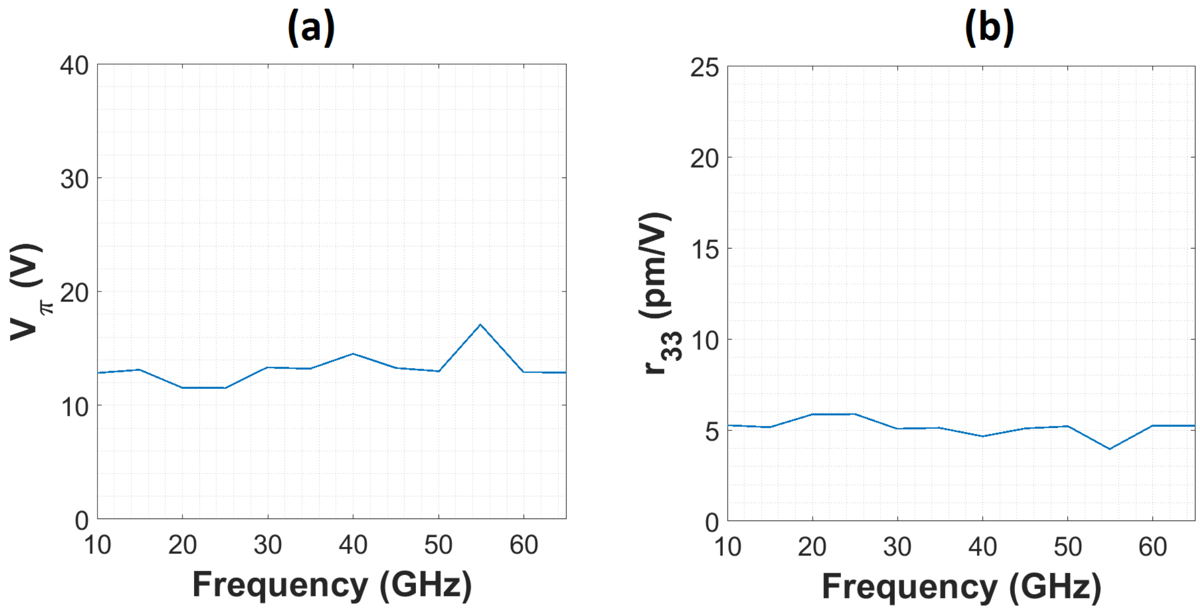

Figure 5.10: (a) V_π and (b)r_{33}

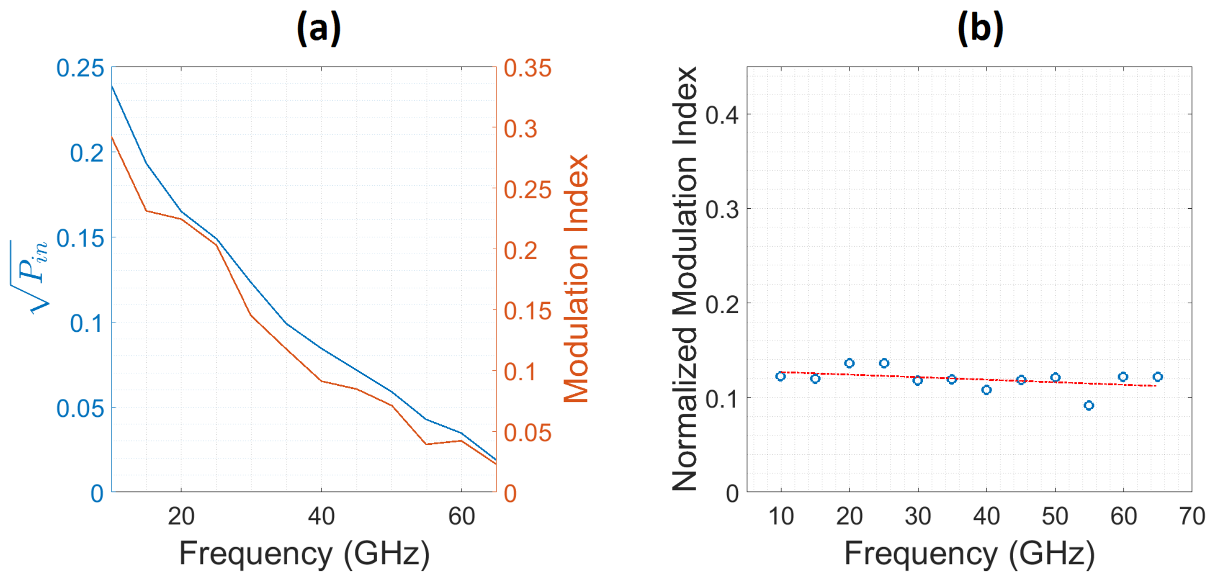

Figure 5.11: $\sqrt{P_{in}}$ & modulation index and (b) normalized modulation index of BTO MZM

Chapter 6

Summary and Outlook

In this work, the dielectric property determination procedure of a high-K thin film for broadband microwave frequencies is presented. The optical property of the thin film is measured using an Ellipsometer. The optical properties and the dielectric properties of the thin film were used to design a CC-SOH modulator. The modulators having different dimensions have been fabricated and the bandwidth measurement was done for some fabricated devices. The main goal of this thesis was to enhance the bandwidth of an SOH modulator. It has been observed that, the 3 dB bandwidth of the modulator is at least 65 GHz which is undoubtedly a very good result.

Nevertheless, there is a lot of room for improvement of the CC-SOH modulator. The best poling efficiency could not be achieved because of the maximum voltage range of the precision source (210 V). After performing a perfectly optimized poling process a numerical value for the 3 dB bandwidth of the fabricated modulator can be measured. The bandwidth measurement for a CC-SOH modulator having lower thickness of $BaTiO_3$ (50 nm) was done. But the modulator is supposed to give even better results for higher thickness of $BaTiO_3$. Therefore, the characterization for CC-SOH modulator having a higher $BaTiO_3$ thickness has to be conducted. Besides, the dielectric constant extraction procedure has to be improved so that, the transmission line for feeding the RF signals can be optimized perfectly for 50 Ω. The device capacitances were not estimated yet that is very necessary to present an analytical model of the CC-SOH model. Additionally, the $BaTiO_3$ sputtering process was not optimized. This is necessary to avoid the side-wall deposition of $BaTiO_3$. If the aforementioned steps are taken then indisputably the CC-SOH modulator will be one of the fastest compact EO modulators.

Appendix A

Ellipsometry

The optical characteristics (complex refractive index) of a thin film can be investigated by a technique called *Ellipsometry.* In this technique the change of polarization is measured upon reflection or transmission and compared to a model. In our experiments, the reflection type Ellipsometry was used and the experimental data were compared to Cauchy's dispersion equation [58]. The spectroscopic setup which performs ellipsometry is known as an Ellipsometer.

A.1 Experimental Setup

A schematic setup of an Ellipsometer is shown in Figure A.1. Electromagnetic radiation is emitted by a tunable light source. The input radiation is linearly polarized which falls onto the sample. The reflected light passes through an analyzer and finally detected by a detector.

A.2 Data Acquisition and Analysis

Using the setup described in Figure A.1 the complex reflectance ratio, ρ is measured. The reflectance ratio can be expressed by the amplitude component, Ψ and the phase difference, Δ. The light incident on the sample is linearly polarized and hence can be decomposed into two polarization states called *s-polarization* and *p-polarization.* The *s-polarized* oscillates perpendicular to the plane of incidence and parallel to the sample surface. The *p-polarized*

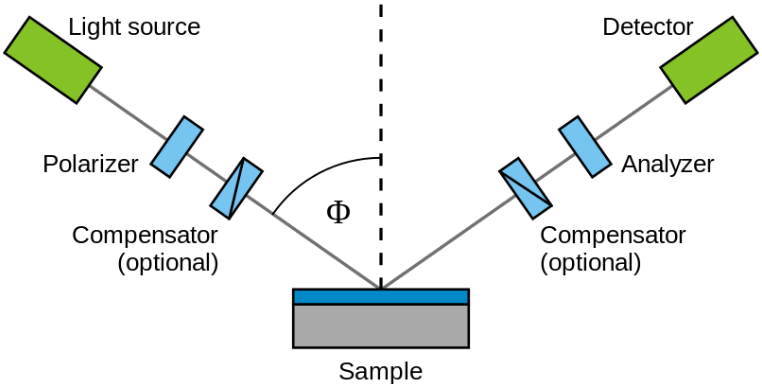

Figure A.1: schematic diagram of Ellipsometer

light oscillates parallel to the plane of incidence. If the normalized reflectances of the *s-polarized* and *p-polarized* lights after reflection are r_s and r_p respectively then the complex reflectance ratio is,

$$\rho = \frac{r_p}{r_s} = tan(\Psi)e^{j\Delta} \tag{A.1}$$

Ellipsometry cannot convert the measured Ψ & Δ values to the refractive index of a thin film in the optical frequency range. Generally the measured Ψ & Δ values are used to fit to an established model. In our experiments the Cauchy dispersion model [58] was used.

$$n(\lambda) = n_0 + C_0\frac{n_1}{\lambda^2} + C_1\frac{n_2}{\lambda^4} \tag{A.2}$$

$$k(\lambda) = k_0 + C_0\frac{k_1}{\lambda^2} + C_1\frac{k_2}{\lambda^4} \tag{A.3}$$

Here, $C_0 = 10^2$ & $C_1 = 10^7$ and wavelength, λ is expressed in *nm*. The n_0 (k_0) value is a constant and wavelength independent. But n_1 (k_1) and n_2 (k_2) values are wavelength dependent. Equation A.2 and A.3 defines the refractive index and the extinction coefficient of the thin film respectively.

Appendix B

Calculation of Different Optical Losses

As described in Section 5.1, there are different optical losses before and after the modulator. These possible losses are the strip waveguide loss, the slot waveguide loss, the grating coupler loss, the strip-to-slot mode converter loss and the MMI loss. Some loss structures were fabricated on the same chip while fabricating the BTO MZMs.

B.1 Strip Waveguide Loss, Grating Coupler Loss & Slot Waveguide Loss

There are strip waveguides of different lengths 250 μm, 500 μm, 1 mm, 3 mm and 5 mm (Figure B.1 (a)). The strip waveguide having a shorter length should have a lower loss than that of a longer one. The loss difference between two different strip waveguides is divided by the consecutive length difference (Equation B.1). The strip waveguide loss is,

$$R_{strip,i} = \frac{R_{strip(measured),2} - R_{strip(measured),1}}{l_{strip,2} - l_{strip,1}} \tag{B.1}$$

Here, $R_{strip(measured),1}$ and $R_{strip(measured),2}$ are the losses which are measured for two of the strip waveguide loss structures with different lengths $lstrip, 1$ and $lstrip, 2$ respectively (depicted in Figure B.1 (a)). The same thing was done for all possible combinations of strip waveguides. Then all the correct combinations were averaged to get the strip waveguide

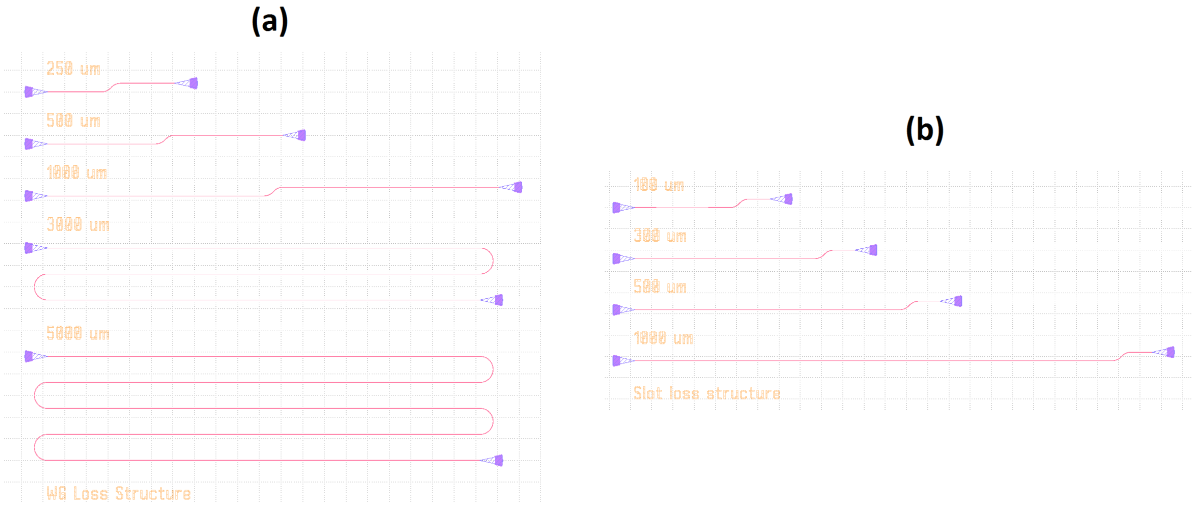

Figure B.1: Loss structures for measuring (a) strip waveguide loss & grating coupler loss and (b) slot waveguide loss

loss (in dB/mm) accurately (Equation B.2).

$$R_{strip} = \frac{\sum_{i=1}^{n} R_{strip,i}}{n} \tag{B.2}$$

The loss, $R_{strip(measured)}$ contains the loss from both the strip waveguide and the grating coupler. So the strip waveguide loss is eliminated from $R_{strip(measured)}$ to get the grating coupler losses for different strip waveguide loss structures (Equation B.3). Then these losses are averaged to get the actual grating coupler loss, RGC (Equation B.4).

$$R_{GC,i} = R_{strip(measured),i} - \left(l_{strip,i} \times R_{strip}\right) \tag{B.3}$$

$$R_{GC} = \frac{\sum_{i=1}^{n} R_{GC,i}}{n} \tag{B.4}$$

There are also some loss structures to measure the slot waveguide loss (Figure B.1 (b)). There are four different lengths (100 μm, 300 μm, 500 μm and 1 mm) of slot waveguides to measure the strip waveguide slot. The slot waveguide loss (R_{slot}) was calculated exactly in the same way how the strip waveguide loss was calculated (using Equation B.5 and B.6).

$$R_{slot,i} = \frac{R_{slot(measured),2} - R_{slot(measured),1}}{l_{slot,2} - l_{slot,1}} \tag{B.5}$$

$$R_{slot} = \frac{\sum_{i=1}^{n} R_{slot,i}}{n} \tag{B.6}$$

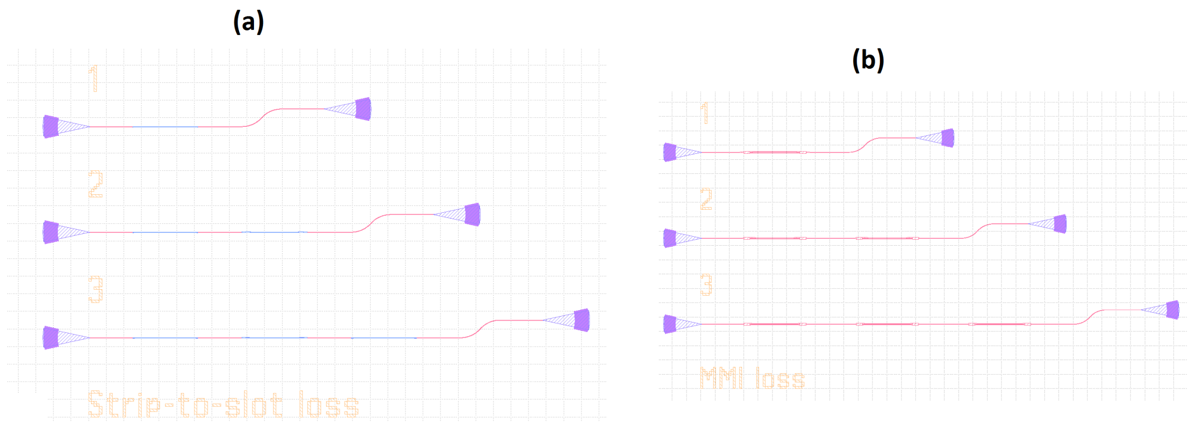

Figure B.2: Loss structures for measuring (a) strip-to-slot mode converter loss & (b) MMI loss

B.2 Strip-to-Slot Mode converter Loss & MMI Loss

There are different structures for measuring the strip-to-slot mode converter loss, $R_{strip-to-slot}$ (Figure B.2 (a)). Two strip-to-slot mode converter pairs are connected with a 50 μm ($l_{strip,connect}$) strip waveguide and each pair of the strip-to-slot mode converters is connected by a 50 μm ($l_{slot,connect}$) slot waveguide. So the measured loss, $R_{strip-to-slot(measured)}$ contains the strip waveguide loss (R_{strip}), the slot waveguide loss (R_{slot}) and the grating coupler loss (R_{GC}). To get the actual loss for each of the strip-to-slot mode converters these losses has to be subtracted and divided by the number of strip-to-slot mode converters, $n_{strip-to-slot}$ (Equation B.7). This was done for all the loss structures and averaged to get the accurate value of $R_{strip-to-slot}$ (Equation B.8).

$$R_{strip-to-slot,i} = \left[\frac{R_{strip-to-slot(measured),i} - \left(\frac{n_{strip-to-slot,i}}{2} - 1\right)\left(l_{strip,connect} \times R_{strip} + l_{slot,connect} \times R_{slot}\right) - 2R_{GC}}{n_{strip-to-slot,i}} \right] \tag{B.7}$$

$$R_{strip-to-slot} = \frac{\sum_{i=1}^{n} R_{strip-to-slot,i}}{n} \tag{B.8}$$

In the similar fashion, the MMI loss is also calculated using Equation B.9 & B.10.

$$R_{MMI,i} = \frac{R_{MMI(measured),i} - \left(\frac{n_{MMI,i}}{2} - 1\right)\left(l_{strip,connect} \times R_{strip}\right) - 2R_{GC}}{n_{MMI,i}} \tag{B.9}$$

$$R_{MMI} = \frac{\sum_{i=1}^{n} R_{MMI,i}}{n} \tag{B.10}$$

Appendix C

Calculation of Modulation Index (m), Half-wave Voltage (V_π) and EO Coefficient (r_{33})

A high speed electro-optic Mach-Zehnder modulator can be characterized using the spectrum of its modulated output optical signal [59]. A very familiar way of characterization of an EO MZM is to measure the modulation index, m from the first side band to the carrier intensity ratio, $R_{1,0}$.

In Figure C.1, a schematic diagram of an imbalance MZM while applying an RF modulating signal is shown. ω_c and ω_m are the optical carrier frequency and the frequency of the modulating RF signal. If the input optical signal is expressed as E_{in} and $\Delta\phi$ is the optical path difference in the two branches of the MZM then the output modulated optical signal, E_{out} can be expressed as,

$$E_{out} = \frac{E_{in}}{2} e^{j\omega_c t} \left[e^{jmcos(\omega_m t)} + e^{-jmcos(\omega_m t) + j\Delta\phi} \right] \tag{C.1}$$

Equation C.1 is then expressed by JacobiAnger expansion which is shown in Equation C.2.

$$E_{out} = \frac{E_{in}}{2} e^{j\omega_c t} \sum_{-\infty}^{\infty} j^k \left[J_k(m) + J_k(-m) e^{j\Delta\phi} \right] e^{jk\omega_m t} \tag{C.2}$$

J_k is the Bessel function of first kind. The intensity of side bands and the carrier signal

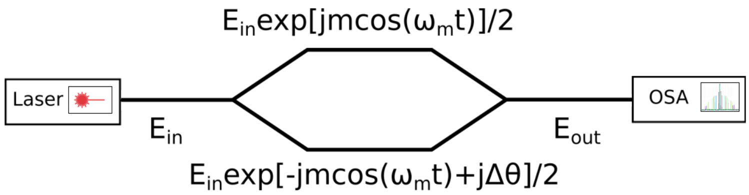

Figure C.1: An imbalanced MZM operating at push-pull mode [60]

can be deduced to,

$$I\big(\omega_c + k\omega_m\big) = \frac{I_{in}}{2} J_k^2(m)\Big[1 + (-1)^k cos(\Delta\phi)\Big] \tag{C.3}$$

When, the intensities of the first sideband (FSB) and carrier signal is considered then $R_{1,0}$ becomes,

$$R_{1,0} = \left[tan^2\Big(\frac{\Delta\phi}{2}\Big)\frac{J_1(m)}{J_0(m)}\right]^2 \tag{C.4}$$

For an SOH modulator $tan(\Delta\phi/2)$ can be safely considered to be 1. This condition was used for CC-SOH modulators as well. Then $R_{1,0}$ becomes,

$$R_{1,0} = \left[\frac{J_1(m)}{J_0(m)}\right]^2 \tag{C.5}$$

Solving the Equation C.5, the modulation index, m was calculated. The V_π was calculated using Equation C.6.

$$V_\pi = \frac{V_m}{m}\pi \tag{C.6}$$

V_m is found from the input power, P_{in} of the RF signal (using $R_t = 50\ \Omega$).

$$P_{in} = \frac{V_m^2}{2R_t} \tag{C.7}$$

The electro-optic (EO) coefficient, r_{33} of an MZM can be found from Equation 2.28.

$$r_{33} = \frac{\lambda_c w_{slot}}{\Gamma_{slot} n_{EO}^3 V_\pi L} \tag{C.8}$$

Here, n_{EO} ($\sim$ 1.67) is the refractive index of the EO polymer (Yoko-2.1) and L is the length of the modulator. Γ_{slot} is known as the field interaction factor which is calculated in the same way as it is done for a conventional SOH modulator [18]. The calculated field interaction factor for the characterized CC-SOH modulator is 0.3427.

$$\Gamma_{slot} = \frac{c\epsilon_0 n_{EO} \iint_{D_{slot}} \mid \underline{E}_{0,x} \mid^2 dxdy}{\iint_{-\infty}^{\infty} Re\big[\underline{E}_0(x,y) \times \underline{H}_0^*(x,y)\big].\vec{e}_z dxdy} \tag{C.9}$$

Bibliography

[1] J. Leuthold, C. Koos, W. Freude, L. Alloatti, R. Palmer, D. Korn, J. Pfeifle, M. Lauermann, R. Dinu, S. Wehrli, M. Jazbinsek, P. Gnter, M. Waldow, T. Wahlbrink, J. Bolten, H. Kurz, M. Fournier, J. M. Fedeli, H. Yu, and W. Bogaerts, "Silicon-organic hybrid electro-optical devices," *IEEE Journal of Selected Topics in Quantum Electronics*, vol. 19, pp. 114–126, Nov 2013. iii

[2] F. Idachaba, D. U. Ike, and O. Hope, "Future trends in fiber optics communication," in *Proceedings of the World Congress on Engineering 2014 Vol I, WCE '14, July 2 - 4, 2014, London, U.K.* (S. I. Ao, L. Gelman, D. W. Hukins, A. Hunter, and A. M. Korsunsky, eds.), Lecture Notes in Engineering and Computer Science, pp. 438–442, International Association of Engineers, Newswood Limited, 2014. 1

[3] G. T. Reed, G. Mashanovich, F. Y. Gardes, and D. J. Thomson, "Silicon optical modulators," *Nature Photonics*, vol. 4, no. 8, pp. 518–526, 2010. 1

[4] D. J. Thomson, F. Y. Gardes, J. M. Fedeli, S. Zlatanovic, Y. Hu, B. P. P. Kuo, E. Myslivets, N. Alic, S. Radic, G. Z. Mashanovich, and G. T. Reed, "50-gb/s silicon optical modulator," *IEEE Photonics Technology Letters*, vol. 24, pp. 234–236, Feb 2012. 1

[5] L. L. Steinmetz, T. W. Pouliot, and B. C. Johnson, "Cylindrical, ring-electrode kd∗p electrooptic modulator," *Appl. Opt.*, vol. 12, pp. 1468–1471, Jul 1973. 1

[6] E. A. West, "Extending the field of view of kd∗p electrooptic modulators," *Appl. Opt.*, vol. 17, pp. 3010–3013, Sep 1978. 1

[7] G. Zheng, J. Xu, L. Chen, H. Wang, and W. She, "Athermal design for the potassium titanyl phosphate electro-optical modulator," *Appl. Opt.*, vol. 46, pp. 6774–6778, Sep 2007. 1

[8] E. L. Wooten, K. M. Kissa, A. Yi-Yan, E. J. Murphy, D. A. Lafaw, P. F. Hallemeier, D. Maack, D. V. Attanasio, D. J. Fritz, G. J. McBrien, and D. E. Bossi, "A review of lithium niobate modulators for fiber-optic communications systems," *IEEE Journal of Selected Topics in Quantum Electronics*, vol. 6, pp. 69–82, Jan 2000. 1

[9] E. L. Wooten, K. M. Kissa, A. Yi-Yan, E. J. Murphy, D. A. Lafaw, P. F. Hallemeier, D. Maack, D. V. Attanasio, D. J. Fritz, G. J. McBrien, and D. E. Bossi, "A review of lithium niobate modulators for fiber-optic communications systems," *IEEE Journal of Selected Topics in Quantum Electronics*, vol. 6, pp. 69–82, Jan 2000. 1

[10] S. Haxha, B. M. A. Rahman, and K. T. V. Grattan, "Bandwidth estimation for ultra-high-speed lithium niobate modulators," *Appl. Opt.*, vol. 42, pp. 2674–2682, May 2003. 1

[11] R. Soref and B. Bennett, "Electrooptical effects in silicon," *IEEE Journal of Quantum Electronics*, vol. 23, pp. 123–129, January 1987. 1

[12] G. T. Reed and A. P. Knights, *A Selection of Photonic Devices*, pp. 145–190. John Wiley Sons, Ltd, 2005. 1

[13] W. M. J. Green, M. J. Rooks, L. Sekaric, and Y. A. Vlasov, "Ultra-compact, low rf power, 10 gb/s silicon mach-zehnder modulator," *Opt. Express*, vol. 15, pp. 17106–17113, Dec 2007. 2

[14] L. R. Dalton, P. A. Sullivan, and D. H. Bale, "Electric field poled organic electro-optic materials: State of the art and future prospects," *Chemical Reviews*, vol. 110, no. 1, pp. 25–55, 2010. PMID: 19848381. 2

[15] R. Spreiter, C. Bosshard, F. Pan, and P. Günter, "High-frequency response and acoustic phonon contribution of the linear electro-optic effect in dast," *Opt. Lett.*, vol. 22, pp. 564–566, Apr 1997. 2

[16] S. Koeber, R. Palmer, M. Lauermann, W. Heni, D. L. Elder, D. Korn, M. Woessner, L. Alloatti, S. Koenig, P. C. Schindler, H. Yu, W. Bogaerts, L. R. Dalton, W. Freude, J. Leuthold, and C. Koos, "Femtojoule electro-optic modulation using a silicon-organic hybrid device," *Light: Science and Applications*, vol. 4, no. 2, 2015. 2

[17] C. Hoessbacher, A. Josten, B. Baeuerle, Y. Fedoryshyn, H. Hettrich, Y. Salamin, W. Heni, C. Haffner, C. Kaiser, R. Schmid, D. L. Elder, D. Hillerkuss, M. Möller,

L. R. Dalton, and J. Leuthold, "Plasmonic modulator with >170 ghz bandwidth demonstrated at 100 gbd nrz," *Opt. Express*, vol. 25, pp. 1762–1768, Feb 2017. 2

[18] C. Koos, J. Leuthold, W. Freude, M. Kohl, L. Dalton, W. Bogaerts, A. L. Giesecke, M. Lauermann, A. Melikyan, S. Koeber, S. Wolf, C. Weimann, S. Muehlbrandt, K. Koehnle, J. Pfeifle, W. Hartmann, Y. Kutuvantavida, S. Ummethala, R. Palmer, D. Korn, L. Alloatti, P. C. Schindler, D. L. Elder, T. Wahlbrink, and J. Bolten, "Silicon-organic hybrid (soh) and plasmonic-organic hybrid (poh) integration," *Journal of Lightwave Technology*, vol. 34, pp. 256–268, Jan 2016. 2, 58

[19] J. Leuthold, W. Freude, J. M. Brosi, R. Baets, P. Dumon, I. Biaggio, M. L. Scimeca, F. Diederich, B. Frank, and C. Koos, "Silicon organic hybrid technology x2014;a platform for practical nonlinear optics," *Proceedings of the IEEE*, vol. 97, pp. 1304–1316, July 2009. 2

[20] R. Palmer, *Silicon photonic modulators for low-power applications.* PhD thesis, Karlsruhe Institute of Technology, 2015. 2, 8, 10

[21] L. Alloatti, R. Palmer, S. Diebold, K. P. Pahl, B. Chen, R. Dinu, M. Fournier, J. M. Fedeli, T. Zwick, W. Freude, C. Koos, and J. Leuthold, "100 GHz silicon-organic hybrid modulator," *Light: Science and Applications*, vol. 3, no. March, pp. 5–8, 2014. 2

[22] R. W. Boyd, *Nonlinear Optics, Third Edition.* Academic Press, 3rd ed., 2008. 3, 5

[23] J.-M. Brosi, *Slow-light photonic crystal devices for high-speed optical signal processing.* PhD thesis, Karlsruhe Institute of Technology, 2009. 7

[24] Q. Xu, V. R. Almeida, R. R. Panepucci, and M. Lipson, "Experimental demonstration of guiding and confining light in nanometer-size low-refractive-index material," *Opt. Lett.*, vol. 29, pp. 1626–1628, Jul 2004. 7

[25] B. E. A. Saleh and M. C. Teich, *Polarization and Crystal Optics*, pp. 193–237. John Wiley Sons, Inc., 2001. 9

[26] L. Alloatti, D. Korn, D. Hillerkuss, T. Vallaitis, J. Li, R. Bonk, R. Palmer, T. Schellinger, A. Barklund, R. Dinu, J. Wieland, M. Fournier, J. Fedeli, P. Dumon, R. Baets, C. Koos, W. Freude, and J. Leuthold, "40 gbit/s silicon-organic hybrid (soh) phase modulator," in *36th European Conference and Exhibition on Optical Communication*, pp. 1–3, Sept 2010. 10

[27] R. Palmer, L. Alloatti, D. Korn, P. C. Schindler, R. Schmogrow, W. Heni, S. Koenig, J. Bolten, T. Wahlbrink, M. Waldow, H. Yu, W. Bogaerts, P. Verheyen, G. Lepage, M. Pantouvaki, J. V. Campenhout, P. Absil, R. Dinu, W. Freude, C. Koos, and J. Leuthold, "Silicon-organic hybrid mzi modulator generating ook, bpsk and 8-ask signals for up to 84 gbit/s," *IEEE Photonics Journal*, vol. 5, pp. 6600907–6600907, April 2013. 10

[28] D. Korn, R. Palmer, H. Yu, P. C. Schindler, L. Alloatti, M. Baier, R. Schmogrow, W. Bogaerts, S. K. Selvaraja, G. Lepage, M. Pantouvaki, J. M. Wouters, P. Verheyen, J. V. Campenhout, B. Chen, R. Baets, P. Absil, R. Dinu, C. Koos, W. Freude, and J. Leuthold, "Silicon-organic hybrid (soh) iq modulator using the linear electro-optic effect for transmitting 16qam at 112 gbit/s," *Opt. Express*, vol. 21, pp. 13219–13227, Jun 2013. 10

[29] D. J. R. Appleby, N. K. Ponon, K. S. K. Kwa, S. Ganti, U. Hannemann, P. K. Petrov, N. M. Alford, and A. O'Neill, "Ferroelectric properties in thin film barium titanate grown using pulsed laser deposition," *Journal of Applied Physics*, vol. 116, no. 12, p. 124105, 2014. 14

[30] S. Roberts, "Dielectric and piezoelectric properties of barium titanate," *Phys. Rev.*, vol. 71, pp. 890–895, Jun 1947. 14

[31] M. S. T. S. C. R. C. M. A. C. J. F. S. Abel, D. Caimi, "Electro-optical properties of barium titanate films epitaxially grown on silicon," 2012. 14

[32] D. W. Richerson, *Modern Ceramic Engineering: Properties, Processing, and Use in Design.* CRC Press, 3^{rd} ed., 2005. 14

[33] L. Mazet, S. M. Yang, S. V. Kalinin, S. Schamm-Chardon, and C. Dubourdieu, "A review of molecular beam epitaxy of ferroelectric batio 3 films on si, ge and gaas substrates and their applications," *Science and Technology of Advanced Materials*, vol. 16, no. 3, p. 036005, 2015. 14

[34] S. Abel, M. Sousa, C. Rossel, D. Caimi, M. D. Rossell, R. Erni, J. Fompeyrine, and C. Marchiori, "Controlling tetragonality and crystalline orientation in batio 3 nano-layers grown on si," *Nanotechnology*, vol. 24, no. 28, p. 285701, 2013. 14

[35] R. Asiaie, W. Zhu, S. A. Akbar, and P. K. Dutta, "Characterization of submicron particles of tetragonal batio3," *Chemistry of Materials*, vol. 8, no. 1, pp. 226–234, 1996. 15

[36] H.-F. Cheng, M.-H. Yeh, K.-S. Liu, and I.-N. Lin, "Characteristics of batio 3 films prepared by pulsed laser deposition," *Japanese Journal of Applied Physics*, vol. 32, no. 12R, p. 5656, 1993. 15

[37] D. J. R. Appleby, N. K. Ponon, K. S. K. Kwa, S. Ganti, U. Hannemann, P. K. Petrov, N. M. Alford, and A. O'Neill, "Ferroelectric properties in thin film barium titanate grown using pulsed laser deposition," *Journal of Applied Physics*, vol. 116, no. 12, p. 124105, 2014. 15

[38] T. Nagatomo, T. Kosaka, S. Omori, and O. Omoto, "Fabrication of batio3 films by rf planar-magnetron sputtering," *Ferroelectrics*, vol. 37, no. 1, pp. 681–684, 1981. 15

[39] J. S. Zhu, X. M. Lu, W. Jiang, W. Tian, M. Zhu, M. S. Zhang, X. B. Chen, X. Liu, and Y. N. Wang, "Optical study on the size effects in batio3 thin films," *Journal of Applied Physics*, vol. 81, no. 3, pp. 1392–1395, 1997. 15

[40] "Materials measurement: Dielectric materials - application brief," *Keysight Technologies*. 15

[41] D. K. Ghodgaonkar, V. V. Varadan, and V. K. Varadan, "Free-space measurement of complex permittivity and complex permeability of magnetic materials at microwave frequencies," *IEEE Transactions on Instrumentation and Measurement*, vol. 39, pp. 387–394, Apr 1990. 16

[42] H. Jin, S. R. Dong, and D. M. Wang, "Measurement of dielectric constant of thin film materials at microwave frequencies," *Journal of Electromagnetic Waves and Applications*, vol. 23, no. 5-6, pp. 809–817, 2009. 16

[43] C. P. Wen, "Coplanar waveguide: A surface strip transmission line suitable for nonreciprocal gyromagnetic device applications," *IEEE Transactions on Microwave Theory and Techniques*, vol. 17, pp. 1087–1090, Dec 1969. 17

[44] X. Wang, *Tunable microwave filters using ferroelectric thin films*. PhD thesis, University of Birmingham, 2009. 17

[45] R. E. Collin, *Foundations for Microwave Engineering*. Wiley-IEEE Press, 2^{nd} ed., 2000. 18

[46] E. Carlsson and S. Gevorgian, "Conformal mapping of the field and charge distributions in multilayered substrate cpws," *IEEE Transactions on Microwave Theory and Techniques*, vol. 47, pp. 1544–1552, Aug 1999. 18

[47] S. Gevorgian, L. J. P. Linner, and E. L. Kollberg, "Cad models for shielded multilayered cpw," *IEEE Transactions on Microwave Theory and Techniques*, vol. 43, pp. 772–779, Apr 1995. 19

[48] W. R. Eisenstadt and Y. Eo, "S-parameter-based ic interconnect transmission line characterization," *IEEE Transactions on Components, Hybrids, and Manufacturing Technology*, vol. 15, pp. 483–490, Aug 1992. 20, 21

[49] H.-T. Lue and T.-Y. Tseng, "Application of on-wafer trl calibration on the measurement of microwave properties of ba/sub 0.5/sr/sub 0.5/tio/sub 3/ films," *IEEE Transactions on Ultrasonics, Ferroelectrics, and Frequency Control*, vol. 48, pp. 1640–1647, Nov 2001. 22

[50] H. M. O'bryan, R. K. Watts, S. Hou, and Z. X. Ma, "Growth and characterization of thin film dielectrics for microwave applications," *Integrated Ferroelectrics*, vol. 15, no. 1-4, pp. 155–162, 1997. 23

[51] T. Hamano, D. J. Towner, and B. W. Wessels, "Relative dielectric constant of epitaxial batio3 thin films in the ghz frequency range," *Applied Physics Letters*, vol. 83, no. 25, pp. 5274–5276, 2003. 23

[52] S. Abel, *Dispositifs électro-optiques à base de Titanate de Baryum épitaxié sur Silicium pour la photonique intégrée.* PhD thesis, Université De Grenoble, 2014. 25

[53] N.-Y. Lee, T. Sekine, Y. Ito, and K. Uchino, "Deposition profile of rf-magnetron-sputtered b a t i o 3 thin films," *Japanese Journal of Applied Physics*, vol. 33, no. 3R, p. 1484, 1994. 25

[54] R. N. Simons, *Coplanar Waveguide with Finite-Width Ground Planes*, pp. 112–126. John Wiley Sons, Inc., 2002. 29

[55] R. Palmer, L. Alloatti, D. Korn, W. Heni, P. C. Schindler, J. Bolten, M. Karl, M. Waldow, T. Wahlbrink, W. Freude, C. Koos, and J. Leuthold, "Low-loss silicon strip-to-slot mode converters," *IEEE Photonics Journal*, vol. 5, pp. 2200409–2200409, Feb 2013. 41

[56] H. Zwickel, S. Wolf, C. Kieninger, Y. Kutuvantavida, M. Lauermann, T. de Keulenaer, A. Vyncke, R. Vaernewyck, J. Luo, A. K.-Y. Jen, W. Freude, J. Bauwelinck, S. Randel, and C. Koos, "Silicon-organic hybrid (soh) modulators for intensity-modulation

/ direct-detection links with line rates of up to 120 gbit/s," *Opt. Express*, vol. 25, pp. 23784–23800, Oct 2017. 46

[57] F. Qiu, H. Miura, A. M. Spring, J. Hong, D. Maeda, M. aki Ozawa, K. Odoi, and S. Yokoyama, "An electro-optic polymer-cladded tio2 waveguide modulator," *Applied Physics Letters*, vol. 109, no. 17, p. 173301, 2016. 46

[58] F. A. Jenkins and H. E. White, *Fundamentals of Optics*. McGraw-Hill, 4^{th} ed., 1981. 50, 51

[59] Y. Shi, L. Yan, and A. E. Willner, "High-speed electrooptic modulator characterization using optical spectrum analysis," *Journal of Lightwave Technology*, vol. 21, pp. 2358–2367, Oct 2003. 56

[60] Z. Li, "THz Plasmonic Modulators," Master's thesis, Karlsruhe Institute of Technology, 2016. 57